Nucleic Acids Research Advance Access published February 24, 2012

Nucleic Acids Research, 2012, 1–17
doi:10.1093/nar/gks138

Single-molecule multiparameter fluorescence spectroscopy reveals directional MutS binding to mismatched bases in DNA

Michele Cristóvão[1,2], Evangelos Sisamakis[3,4], Manju M. Hingorani[5], Andreas D. Marx[1], Caroline P. Jung[1], Paul J. Rothwell[3,*], Claus A. M. Seidel[3,*] and Peter Friedhoff[1,*]

[1]Institute for Biochemistry, FB 08, Justus Liebig University, Heinrich-Buff Ring 58, D-35392 Giessen, Germany, [2]Department of Cell Biology and Genetics, Erasmus Medical Center, Dr. Molewaterplein 50, 3015 GE Rotterdam, The Netherlands, [3]Molecular Physical Chemistry, Heinrich-Heine University, Universitätsstrasse 1, 40225 Düsseldorf, Germany, [4]Department of Applied Physics, Experimental Biomolecular Physics, Royal Institute of Technology, SE-106 91 Stockholm, Sweden and [5]Molecular Biology and Biochemistry Department, Wesleyan University, Middletown, CT 06459, USA

Received November 3, 2011; Revised January 20, 2012; Accepted January 23, 2012

ABSTRACT

Mismatch repair (MMR) corrects replication errors such as mismatched bases and loops in DNA. The evolutionarily conserved dimeric MMR protein MutS recognizes mismatches by stacking a phenylalanine of one subunit against one base of the mismatched pair. In all crystal structures of G:T mismatch-bound MutS, phenylalanine is stacked against thymine. To explore whether these structures reflect directional mismatch recognition by MutS, we monitored the orientation of *Escherichia coli* MutS binding to mismatches by FRET and anisotropy with steady state, pre-steady state and single-molecule multiparameter fluorescence measurements in a solution. The results confirm that specifically bound MutS bends DNA at the mismatch. We found additional MutS–mismatch complexes with distinct conformations that may have functional relevance in MMR. The analysis of individual binding events reveal significant bias in MutS orientation on asymmetric mismatches (G:T versus T:G, A:C versus C:A), but not on symmetric mismatches (G:G). When MutS is blocked from binding a mismatch in the preferred orientation by positioning asymmetric mismatches near the ends of linear DNA substrates, its ability to authorize subsequent steps of MMR, such as MutH endonuclease activation, is almost abolished. These findings shed light on prerequisites for MutS interactions with other MMR proteins for repairing the appropriate DNA strand.

INTRODUCTION

The DNA mismatch repair (MMR) system is responsible for detecting and processing numerous discrepancies in DNA, including base pair mismatches and insertion/deletion loops arising from DNA polymerase errors or during homeologous recombination, as well as DNA damage lesions (1). The principal components of MMR, MutS and MutL, are highly conserved proteins that initiate and coordinate the appropriate DNA repair or DNA damage signaling responses. MutS searches for and recognizes mismatches and lesions in DNA, while MutL serves as a molecular matchmaker (and endonuclease in eukaryotes) to direct subsequent steps in the reaction following mismatch/lesion recognition (2,3). In *Escherichia coli*, MMR is directed to the erroneous daughter strand by MutSL-dependent nicking by the strand discrimination endonuclease MutH (4). MutS and MutL are essential for maintaining genome integrity, as illustrated by the fact that many mutations in these proteins are causative of Lynch syndrome in humans (5,6). Initiation of MMR is a complex and dynamic process in which MutS scans vast lengths of duplex DNA to detect relatively infrequent errors, and then generates an error-specific signal to activate MutL, which in turn sets in motion excision of the incorrect DNA strand and subsequent re-synthesis. MutS proteins possess two key activities, the ability to bind DNA and distinguish a variety of non-Watson–Crick structures and an ATPase activity that modulates their interactions with DNA and other proteins during initiation of MMR. In the *E. coli* model system, MutS exists in a homo–dimer/tetramer equilibrium, and the dimeric form of the protein is

*To whom correspondence should be addressed. Tel: +49 641 9935407; Fax: +49 641 9935409; Email: peter.friedhoff@chemie.bio.uni-giessen.de
Correspondence may also be addressed to Claus A. M. Seidel. Tel: +49 211 8115881; Fax: +49 211 8112803; Email: cseidel@hhu.de
Correspondence may also be addressed to Paul J. Rothwell Tel: +49211 8114715; Fax: +49 211 8112803; Email: p.rothwell@mail.cryst.bbk.ac.uk

known to be MMR competent (7–10). In eukaryotes, MutS homologs are hetero-dimeric proteins (e.g. human MSH2/MSH6 or MutSα and MSH2/MSH3 or MutSβ) (11–13).

Crystal structures of various DNA–MutS complexes show a hallmark 45–60° kink in the DNA at the mismatch/lesion target site and very similar mismatch/lesion-specific and non-specific contacts between MutS and DNA (12,14–16). The asymmetry in prokaryotic and eukaryotic MutS dimers and their interactions with DNA revealed by the high-resolution structures is striking; only one subunit of the MutS dimer makes specific contact with only one of the mismatched bases at the target site. A conserved phenylalanine from the Phe-X-Glu-motif in the mismatch-binding domain of *E. coli* MutS A subunit (eukaryotic MSH6) stacks on a mismatched base from one of the DNA strands and the conserved glutamate makes a hydrogen bond with the same base (12,14,15). In principle, MutS could bind a mismatched base pair (e.g. G:T) in two orientations, with Phe stacking either on the mismatched G in the top strand or the mismatched T in the bottom strand. However, in crystal structures of a G:T mismatch bound by *E. coli* MutS and human MutSα, only the T (in the bottom strand) is found stacked with the conserved Phe (12,14). In the crystal structure of *E. coli* MutS bound to G:G, only the G in the bottom strand is bound (recognized) by MutS (15). These structural data suggest an intrinsic bias in the orientation of MutS interaction with mismatched base pairs, which could have significant consequences for the efficacy with which different mismatches are recognized and repaired. Other than the information available from crystal structures, little is known about directional binding of MutS to mismatches. The only in-solution quantitative data available on this issue are from a single-molecule DNA unzipping analysis, in which differences were observed in the peak force values required to disrupt the *Saccharomyces cerevisiae* Msh2–Msh6–G:T complex versus Msh2–Msh6–T:G complex (17). Thus, the question as to whether MutS binding to mismatches is directionally biased in a solution remains to be addressed, as well as the related question of whether MMR is influenced by which base of the mismatch is contacted by the MutS Phe-X-Glu.

In this study, we investigated binding of *E. coli* MutS to DNA containing different mismatches using ensemble fluorescence spectroscopy and single-molecule multiparameter fluorescence detection (smMFD), in order to gain information on the associated structural dynamics (not provided by the static crystal structures) and to specifically address the possibility that MutS binds mismatches with a preferred orientation. We performed the single-molecule fluorescence spectroscopy on free diffusing molecules to avoid possible complications due to unwanted interactions of MutS with the surface. This is the first time that smMFD has been used to study the MutS protein, and this approach allowed us to detect multiple DNA–MutS species that otherwise are not distinguishable in ensemble or other single-molecule studies (18–22). We show that in a solution, MutS does interact with a mismatched base pair in two different orientations and that, depending on the type of mismatch, one orientation is indeed preferred strongly over the other. We discuss the implications of these findings in light of proposed models of the MMR mechanism.

MATERIALS AND METHODS

Proteins

The cysteine-free (CF) *E. coli* MutS dimer variant MutS-CF/D835R was expressed as the His-tagged fusion protein and purified using Ni-NTA affinity chromatography followed by gel filtration (9). Purification of recombinant proteins MutL and MutH was performed essentially as described elsewhere (23–25).

Fluorophore-labeled DNA

The sequences of the 42 bp oligonucleotides used in fluorescence experiments were top strand, 5′-TAT TAA TTT CGC GGG CTC GA*X* AGC TTC ATC CTC TAC GCC GGA-3′ and bottom strand, 5′-TCC GGC GTA GAG GAT GAA GCT *Y*TC GAG CCC GCG AAA TTA ATA-3′. X:Y represents the type of base pair at the central position (e.g. in G:T, X = G and Y = T). Labeled DNA duplexes were prepared by annealing complementary oligonucleotides (Purimex, Germany) containing Alexa Fluor 594 (*A*) at position 9 on the X strand and Alexa Fluor 488 (*D*) on position 8 on the Y strand attached to a thymine via a flexible C6-linker (Figure 1A). See also Figure 6 for additional oligonucleotides used in the study.

Modeling the 42 bp G:T heteroduplex DNA

A 3D model of the 42-bp DNA (X:Y) structure in B-form was generated using the 3D-DART webserver (26). Two structural models of the MutS-bound kinked DNA were generated by using DNA distortion parameters obtained from the NDB server (ndbserver.rutgers.edu) using the crystal structure of MutS and a 30-bp G:T DNA (PDB code 1e3m). Parameters of positions 2–16 from the top strand (chain E) and positions 15–29 from bottom strand (chain F) were used for positions 14–28 of the top strand and positions 57–71 of the bottom strand forming the 42-bp G:T-DNA (positions 57–71 and 14–28 for the T:G DNA, respectively). Parameters for B-DNA (obtained from the 3D-DART webserver, see above) were used for all other positions. Sequence-dependent structural bending of the chosen DNA sequence is not significant as judged by the program DIAMOD (27) MutS was docked to this modeled DNA by superposition of the phosphate backbone atoms of the DNA in the co-crystal structure onto the respective atoms of the modeled DNA using PyMOL (DeLano Scientific LLC, version 1.2r2). The accessible volumes of fluorophores were modeled as described in (28). They are depicted as clouds representing the rotational freedom of the fluorophore dependent on the linker length and steric clashes with the DNA (for details see Supplementary Data Sections 1.1 and 1.2). The distance between mean dye positions R_{mp} was determined as 85 Å

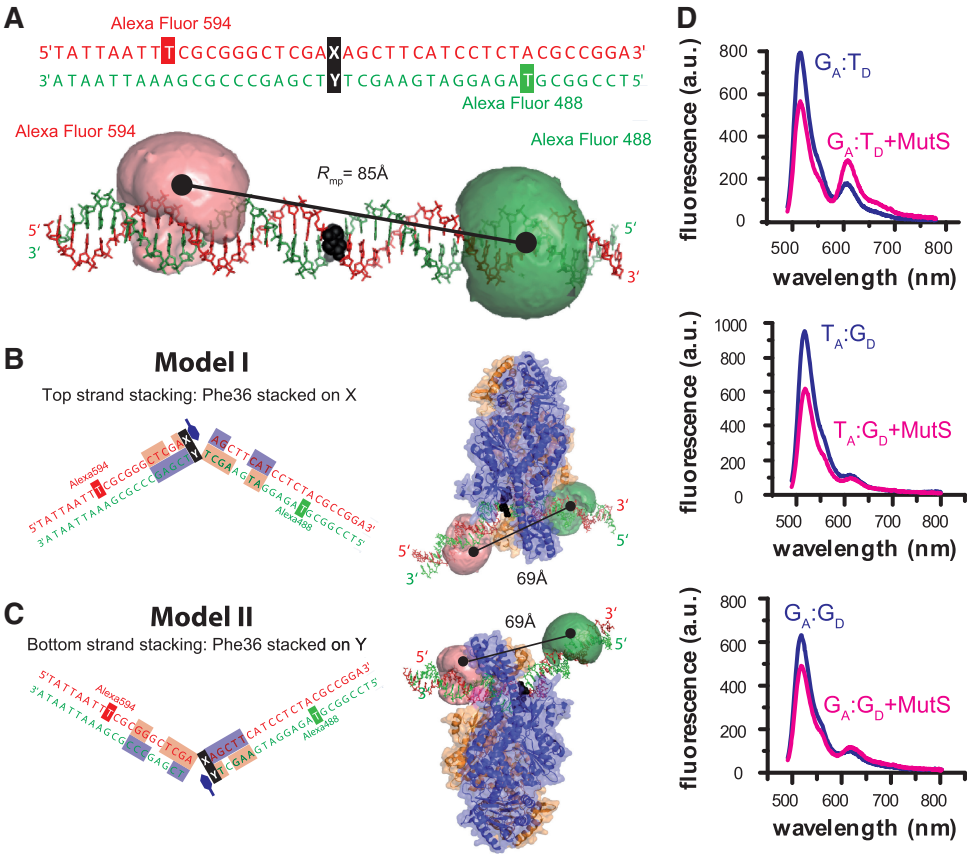

Figure 1. MutS-binding orientation and DNA bending with mismatched DNA monitored by fluorescence spectroscopy. (**A**) Sequence and molecular model of the 42-bp DNA containing a central mismatch (X_A:Y_D, black) and an Acceptor (Alexa Fluor 594, red) and Donor dye (Alexa Fluor 488, green) in the top or bottom strand. In the molecular model the dyes are depicted as clouds, representing possible positions of the freely rotating dye (21). The distance between the mean dye positions is R_{mp} = 85 Å. (**B, C**) Model of the complex between *E. coli* MutS and X_A:Y_D DNA when Phe-36 (indicated with a blue hexagon) is stacked on the mismatched X base (B) or the mismatched Y base (C). Subunit A and B of MutS are shown in blue and orange and the DNA bases interacting which each monomer are shown in blue and orange, respectively. In both binding orientations (B or C), the distance between mean dye positions is R_{mp} = 69 Å; however, only in (B, Model I) the donor dye is in contact with the protein. (**D**) Steady-state fluorescence emission spectra of 10 nM G_A:T_D, T_A:G_D and G_A:G_D in the absence (blue curve) or presence (magenta curve) of 125 nM MutS dimer.

for dsDNA (Figure 1A). The distance dependence for Förster Resonance Energy Transfer (FRET) from an excited *D* molecule to an *A* molecule is given by the Förster equation $E = 1/(1+(R_{DA}/R_0)^6)$, where the FRET efficiency, *E*, is related to distance between *D* and *A*, R_{DA} and the Förster radius R_0 for a specific *DA* pair (for Alexa Fluor 488 (*D*) and Alexa Fluor 594 (*A*) R_0 = 53.2 Å).

However, in FRET experiments not E_{mp} ($E_{mp} = 1/(1+(R_{mp}/R_0)^6)$) but rather a mean FRET efficiency $\langle E\rangle$ is measured, which is an average over all pairs of spatial dye positions, $R_{DA(i)}$, and is given by $\langle E\rangle = \langle R_0^6/R_0^6+R_{DA(i)}^6\rangle$ (21,28) (22). By inserting $\langle E\rangle$ in the Förster equation and solving for the inter-dye distance, the FRET-averaged distance between the dyes $\langle R_{DA}\rangle_E$ can be calculated as $\langle R_{DA}\rangle_E = R_0\ (1/\langle E\rangle - 1)^{1/6}$. The corresponding theoretical values for $\langle E\rangle$ and $\langle R_{DA}\rangle_E$ are denoted as $\langle E\rangle^{model}$ and $\langle R_{DA}\rangle_E^{model}$, respectively. Considering the volume sterically accessible to the dye in the above model of dsDNA, the computed value is $\langle E\rangle^{model} = 0.063$, which corresponds to $\langle R_{DA}\rangle_E^{model} =$ 83 Å (28). In our case, $\langle R_{DA}\rangle_E^{model}$ is close to the R_{mp} = 85 Å. Considering the two MutS:DNA complexes in Figure 1B, we calculate for G_A:T_D and for T_A:G_D bound to MutS nearly identical values of $\langle E\rangle^{model} = 0.20$ and the $\langle R_{DA}\rangle_E^{model}$ = 67 Å, which is close to R_{mp} = 69 Å.

Single-molecule fluorescence spectroscopy

In all experiments, double-labeled DNA (7.5–15 pM) was incubated with MutS (150 nM dimer) in 25 mM Tris (pH7.5), 125 mM KCl and 5 mM $MgCl_2$ and 0.5 mg/ml BSA in the absence or presence of ADP, ATP or AMP-PNP (1 mM). The experiments were carried out with a confocal epi-illuminated set-up (29) with spectral detection windows for donor (520/66 nm) and acceptor (630/60 nm). The fluorescently labeled molecules were excited by a linearly polarized, active-mode-locked Argon-ion laser (476.5 nm, 73 MHz, 150 ps) (see Supplementary Data Section 1.3). Fluorescence bursts are distinguished from the background of 3–3.5 kHz by applying threshold intensity criteria defined by 0.05 ms interphoton time and 100 photons minimum per burst. An additional selection criterion was applied to reduce

the number of bursts containing donor only molecules taken into consideration in the analysis (see Supplementary Data Section 2.1). A detailed description for the calculation for the experimentally recovered FRET parameters is given in Supplementary Data Section 2.2. A description of the fitting procedure for Photon Distribution Analysis (PDA) is given in the Supplementary Data Section 2.3, whereas a detailed description of the analysis techniques can be found in ref. (30,31).

Stopped-flow fluorescence measurements

All experiments were performed in 25 mM Tris (pH 7.5), 125 mM KCl and 5 mM $MgCl_2$ by using an Applied Photophysics SX20 with dual detection stopped flow apparatus (deadtime 1.1 ms), with Alexa Fluor 488 excitation at 493 nm and Alexa Fluor 594 excitation at 593 nm. Donor and acceptor fluorescence was separated by two bandpass filters with the following ranges: HQ 520/35 nm (green) and HQ 645/75 nm (red). The signal was normalized to the maximum of each measurement. Kinetics of MutS binding to G_A:T_D were measured by mixing equal volumes of MutS (500 nM dimer), pre-incubated with nucleotide (2 mM of ADP, ATP or AMP-PNP), with DNA (30 nM) (mixing ratio 1:1). The effect of ATP or ADP on a G_A:T_D–MutS complex was determined by pre-incubating DNA (30 nM) and MutS (500 nM dimer) and challenging the complex with 2 mM of ADP or ATP (mixing ratio 1:1). Dissociation kinetics of MutS from G_A:T_D were measured by mixing preformed G_A:T_D–MutS complex with 75-fold molar excess of a trap (G:T-22, see also Figure 7) and ADP or ATP (mixing ratio 1:1). In all experiments, the final concentrations are 250 nM MutS dimer, 1 mM ATP and 15 nM DNA. The curves were fitted to a single, double or triple exponential using OriginLab 8.5: single: $y = y_0 + Ae^{-x/t}$, double: $y = y_0 + A_1e^{-x/t_1} + A_2e^{-x/t_2}$ or triple: $y = y_0 + A_1e^{-x/t} + A_2e^{-x/t_2} + A_3e^{-x/t_3}$; y_0 corresponds to the offset, A_1, A_2, A_3 correspond to the amplitudes of decay constants t_1, t_2 and t_3 and $t = 1/k_{obs}$.

Steady-state fluorescence measurements

Steady state fluorescence measurements (FRET and anisotropy) were performed by incubating MutS (125 or 250 nM dimer) with double-labeled DNA, X_A:Y_D (10 nM), in 25 mM Tris/HCl, pH 7.5, 125 mM KCl and 5 mM $MgCl_2$ in the absence or presence of ADP (1 mM) for 5 min at 20°C. Fluorescence anisotropy (r) measurements were performed with double- or single-labeled 42-bp DNA as described for the steady-state fluorescence measurements but using the polarization module of Fluoromax 4 with λ_{ex} = 470 nm and λ_{em} = 517 nm for the donor (r_D), and λ_{ex} = 570 nm and λ_{em} = 615 nm for the acceptor (r_A) (1.8 nm slit width; signals averaged for 2 s).

Competition titration experiments

MutS-CF/D835R (50 nM dimer) was pre-incubated with G_A:T_D DNA (50 nM), and the complex was then competed with increasing concentrations of unlabeled 42-bp duplexes containing a G:T or T:G mismatch, 22 or 6 bp from the 3′ end (G:T-22, T:G-22, G:T-6, T:G-6). FRET was monitored at three excitation/emission wavelengths (in nm), F_D (λ_{ex} = 475 / λ_{em} = 525), F_A (575/625) and F_{DA} (475/625), using a Tecan Infinite M200 fluorescence plate reader. F_{DA}/F_A was plotted against the concentration of the competitor and the data were fit using the parameter estimation tool of COPASI (32).

Substrates for MutH activity assays

Long heteroduplex DNA (390 or 406 bp) was generated by annealing two single-stranded DNA fragments generated from PCR products after λ-exonuclease treatment (33). The following primers (biomers.net, Germany) were used for each substrate: **G:T-22-L**, TCA TCC TCG GCA CCG TCA C and **p**-TCC GGC GTA GAG GAT GAA GCT **C**TC GAG CCC GCG AAA TTA ATA (top strand), **p**-TCA TCC TCG GCA CCG TCA C and TCC GGC GTA GAG GAT GAA GCT **T**TC GAG CCC GCG AAA TTA ATA (bottom strand); **G:T-6-L,** TCA TCC TCG GCA CCG TCA C and **p**-AAG CT**C** TCG AGC CCG CGA AAT TAA TAC GAC TCA CTA TAG GGG (top strand) and **p**-TCA TCC TCG GCA CCG TCA C and AAG CT**T** TCG AGC CCG CGA AAT TAA TAC GAC TCA CTA TAG GGG (bottom strand); **T:G-22-L**, TCA TCC TCG GCA CCG TCA C and **p**-TCC GGC GTA GAG GAT GAA GCT **A**TC GAG CCC GCG AAA TTA ATA (top strand) and **p**-TCA TCC TCG GCA CCG TCA C and TCC GGC GTA GAG GAT GAA GCT **G**TC GAG CCC GCG AAA TTA ATA (bottom strand); **T:G-6-L,** TCA TCC TCG GCA CCG TCA C and **p**-AAG CT**A** TCG AGC CCG CGA AAT TAA TAC GAC TCA CTA TAG GGG (top strand) and **p**-TCA TCC TCG GCA CCG TCA C and AAG CT**G** TCG AGC CCG CGA AAT TAA TAC GAC TCA CTA TAG GGG (bottom strand); G:C-22-L, TCA TCC TCG GCA CCG TCA C and **p**-TCC GGC GTA GAG GAT GAA GCT **C**TC GAG CCC GCG AAA TTA ATA (top strand) and **p**-TCA TCC TCG GCA CCG TCA C and TCC GGC GTA GAG GAT GAA GCT **C**TC GAG CCC GCG AAA TTA ATA (bottom strand). **p** stands for a 5′ phosphorylated primer.

Mismatched-provoked activation of MutH by MutS and MutL

MutH endonuclease activation by MutS and MutL was assayed on long DNA substrates (390 or 406 bp) containing a G:T, T:G or G:C base pair at position 385 and a single unmethylated GATC site at position 210. DNA (10 nM) was incubated with MutH (500 nM), MutL (500 nM monomer) and MutS-CF/D835R (250 nM dimer) in 10 mM Tris-HCl (pH 7.9), 5 mM $MgCl_2$, 1 mM ATP and 125 mM KCl at 37°C. DNA substrate and cleavage products were analyzed by 6% polyacrylamide gel electrophoresis followed by ethidium bromide staining. MutH endonuclease activity was scored by the appearance of products from cleavage of both DNA strands at the unmethylated GATC site.

RESULTS AND DISCUSSION

Design and modeling of dye-labeled DNA to study MutS binding and kinking DNA

Binding and bending of mismatched DNA by MutS was monitored using double-labeled DNA and performing bulk or single molecule FRET measurements. We used Alexa Fluor 488 (*D*) and Alexa Fluor 594 (*A*) as a FRET pair (*DA*) attached via a C_6 linker, respectively, to the bottom and top strand of a 42 bp double-stranded oligonucleotide termed X_A:Y_D (Figure 1A). The Förster radius for the specific dye pair at the specific labeling positions was determined to be $R_0 = 53.2$ Å. A molecular model of the dye labeled oligonucleotide in the B-DNA form was generated and the mean dye positions were determined in the volume sterically accessible to the coupled dyes (green and red clouds in Figure 1A, respectively) as described in the Materials and Methods section (21,28,34). According to our model, the FRET-averaged distance between the two fluorophores in free DNA, $\langle R_{DA}\rangle_E^{model}$, is 83 Å and the FRET efficiency, $\langle E\rangle^{model}$, is 0.063.

Next, we modeled the structure of the complex between MutS and the dye-labeled DNA (X_A:Y_D) based on the crystal structure of *E. coli* MutS with a G:T DNA (PDB code 1e3m, (14). We generated two models for X_A:Y_D, in which the conserved Phe-36 in subunit A of MutS stacked either on the mismatched base in the top strand (X) (Model I, Figure 1B) or the bottom strand (Y) (Model II, Figure 1C). In both cases, the FRET-averaged distance, $\langle R_{DA}\rangle_E^{model}$, is expected to shorten from 83 Å for free DNA to 67 Å for MutS-bound DNA. However, differences in dye–protein interactions between the two DNA–MutS complexes are readily apparent. In Model I (Phe-36 stacked on base X; Figure 1B), ~8% of the donor dye cloud is within 5 Å distance to the mismatch-binding domain of MutS subunit B, whereas no contact is detected in Model II (Phe-36 stacked on base Y; Figure 1C). In contrast, 3% and 23% of the acceptor dye cloud is within 5 Å distance to the DNA-binding clamp domains of MutS in Models I and II, respectively. These structural models indicate that (i) the decrease in sterically available volume for the dye molecules and possible quenching effects due to dye–protein interactions could result in changes in fluorescence anisotropy and (ii) differential changes in donor and acceptor fluorescence anisotropy could distinguish the two DNA–MutS complexes from each other. Thus, in addition to FRET serving as a monitor for DNA binding/bending, anisotropy of the donor and acceptor dye emission may serve as a monitor of MutS orientation on DNA.

Escherichia coli MutS exists in dimer/tetramer equilibrium with a reported K_D ranging from 0.2 to 2 μM (7,8). In this study, we used a tetramerization-deficient but fully repair proficient variant of *E. coli* MutS (MutS-CF/D835R) (9,10) to avoid potential complications in data analysis due to binding of MutS tetramers to DNA (35). Steady-state fluorescence spectroscopy experiments with double-labeled DNA containing a G:T, T:G and G:G mismatch (X_A:Y_D format; Figure 1A) displayed low FRET (LF) in the absence of protein (blue curves in Figure 1D), as expected from the large distance between the two dyes shown in the model. Upon addition of 125 nM MutS to the solution, there was a significant increase in energy transfer as indicated by the concomitant decrease of donor and increase of acceptor fluorescence. Only the G_A:T_D–MutS complex showed the high FRET (HF) expected from the structural models described above. In contrast, the T_A:G_D–MutS complex showed only a donor quench and the G_A:G_D–MutS complex showed a weak FRET increase. It should be noted that in the available crystal structures, all three complexes have DNA kinked by 60°; thus, there are subtle conformational differences among these complexes that are not discernible in crystal structures. Since bulk FRET measurements could not allow us to distinguish different populations of free and bound DNA, we performed a more detailed analysis using smMFD as described below.

smMFD analysis of free DNA

In order to directly detect the heterogeneity of distinct DNA–MutS complexes, we employed a single-molecule approach coupled with MFD. smMFD experiments avoid ensemble averaging by counting and analyzing single-molecule events one at a time. As outlined above, our experimental setup was designed to monitor DNA–MutS complexes by differences in FRET between two dye molecules, and sense orientation-specific binding of MutS to DNA by changes in fluorescence anisotropy (Figure 1). In our single-molecule fluorescence microscope, individually labeled DNA molecules (15 pM) freely diffuse through a confocal detection volume and generate brief bursts of fluorescence over the short dwell time (~1 ms). During these transits, fluorescence intensities (*F*), lifetimes (τ), anisotropies (*r*) and diffusion times of both the donor (*D*) and acceptor (*A*) dyes are probed. The selected bursts are characterized offline to determine all fluorescence parameters. In this work, we performed MFD analysis in two steps. In Step 1, we generated 2D fluorescence parameter histograms of single-molecule bursts (MFD plot) to gain a semi-quantitative overview of distinct species with distinct apparent mean FRET efficiencies $\langle E_a\rangle$ and donor anisotropies r_D (Figure 2A–E). In Step 2, PDA was used for a quantitative and rigorous analysis of the apparent mean FRET efficiency probability distributions to calculate also the corresponding inter-dye distances $\langle R_{DA}\rangle_E$ (Figure 2F–J). In addition, PDA allows us to determine the actual number of species in a probability distribution by considering the stochastic character of photon emission, which leads to the broadening of the observed $\langle E_a\rangle$ distributions (photon shot noise) (see Supplementary Data Section 2.3) (20). Due to the presence of many similar species, we preferred an analysis procedure (for all details see Supplementary Data Section 2.3: fit model 2), where the relevant FRET states were identified from the measurements in which they were predominant and thus able to be characterized with high confidence (see Supplementary Tables S1.4–S1.6). In a joint analysis of all histograms, the PDA fits were most stable, when only relative species fractions were left to vary, i.e. we used fixed distances and variable fractions. Using both 2D

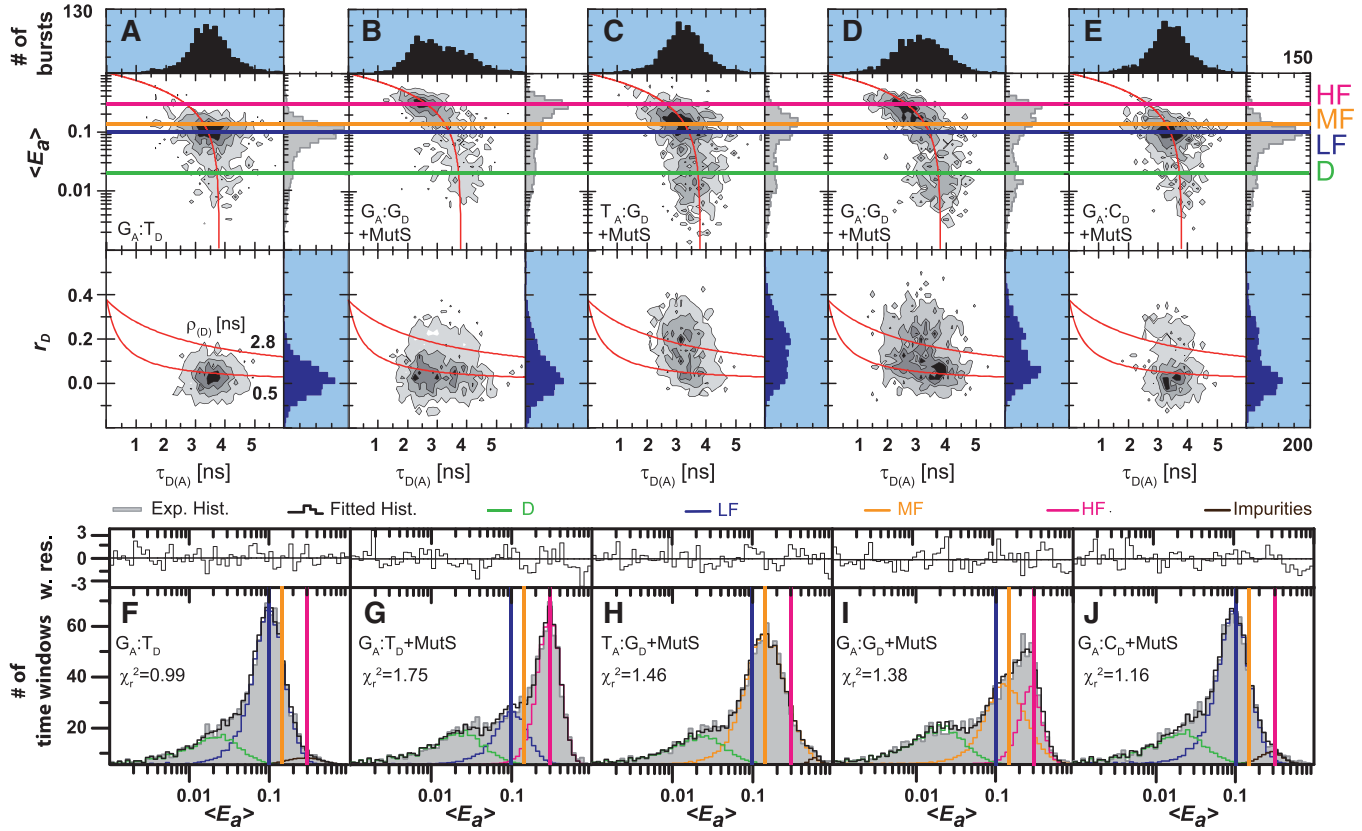

Figure 2. smMFD analysis reveals directional MutS binding on mismatched DNA. Two-dimensional fluorescence parameter histograms counting single-molecule burstsfor smMFD measurements of free DNA (**A**) and MutS bound to different DNA substrates (**B–E**). In the MFD plots, the number of molecules (fluorescence bursts) in each bin is gray-scale coded from white (lowest) to black (highest) and it is normalized to a total of 1000 bursts. The MFD plots are linked by sharing the same *x*-axis: (*Top panel*) Apparent FRET efficiency $\langle E_a \rangle$ is plotted versus $\tau_{D(A)}$ (Donor lifetime in the presence of Acceptor) and (*Bottom panel*) donor anisotropy r_D is plotted versus $\tau_{D(A)}$. $\langle E_a \rangle$ was obtained from raw signals (S) by correcting for green and red background fluorescence, spectral cross-talk ($\alpha = 0.057$), detection efficiencies ($g_G/g_R = 0.78$) and the fluorescence quantum yields ($\Phi_{F(D)} = 0.6$ and $\Phi_{F(A)} = 0.9$) (see Supplementary Data Section 2.3) In the top panel, the red curve illustrates the static FRET line, $E_a = 1-(\tau_{D(A)}/\tau_{D(0)})$, where $\tau_{D(0)} = 3.8$ ns is the fluorescence lifetime of donor in the absence of acceptor. The mean $\langle E_a \rangle$ of the different populations and donor only is shown by the magenta, HF, orange (Middle Fret, MF), blue (LF) and green (donor only, D) lines, respectively. In the bottom panel, the red lines illustrate the Perrin equation ($r_D = r_0/(1+\tau_{D(A)}/\rho_D)$), using a value for fundamental anisotropy of $r_0 = 0.37$ and a mean rotational correlation time, ρ_D, of either 0.5 ns or 2.8 ns, corresponding to the mean values of ρ_D for G_A:T_D–MutS (B) and T_A:G_D–MutS (C), respectively. The additional population observed at $r_D = 0.2$ in the T_A:G_D but not the G_A:T_D data is indicative of differential donor–MutS interactions. (F–J): PDA of $\langle E_a \rangle$ of free DNA (F) and MutS bound to G_A:T_D (G), T_A:G_D (H), G_A:G_D (I) and G_A:C_D (J) with the data histogram in gray for 2 ms time windows. The data were fit to a three state model (Fitmodel 2, see Supplementary Data Section 2.3.1.) which accounts for D and either MF and HF (T_A:G_D–MutS, G_A:G_D–MutS) or LF and HF (G_A:T_D–MutS, G_A:T_D, and G_A:C_D–MutS). The PDA model functions of the fits were constituted by Gaussian distribution of inter-dye distances, with mean distance $\langle R_{DA} \rangle_E$, half-width HW and amplitude A (Supplementary Tables S1.1 and S1.7). The corresponding efficiency distributions were calculated by the retrieved model functions and equation $E = 1/(1+(R_{DA}/R_0)^6$. Reduced chi-square values (ϕ_r^2) and the residuals for each fit are indicated in the respective panel (see Supplementary Data Section 2 for Supporting Theory for FRET Analysis). A correction for the exact treatment of direct excitation was performed according to equation 18.33 in Sisamakis *et al* by additional accounting for a probability of direct acceptor excitation of $p_{DE} = 3.5\%$ (22), so that most accurate distances should be obtained. Populations present in G_A:T_D and T_A:G_D data merge with those in the G_A:G_D data, consistent with MutS binding this symmetric mismatch in both orientations.

analysis and PDA yields unsurpassed sensitivity for characterization of FRET populations derived from single-molecule FRET experimental data (22). It is important to note that in MFD- and PDA-plots, the apparent FRET efficiency $\langle E_a \rangle$ is displayed without correcting for direct acceptor excitation so that the apparent FRET efficiencies in MFD-plots are slightly higher than the FRET efficiencies $\langle E \rangle$, which are related to interesting FRET average inter-dye distances $\langle R_{DA} \rangle_E$. In the calculation of $\langle R_{DA} \rangle_E$ by PDA, the correction for direct excitation is implemented. The differences between $\langle E_a \rangle$ and $\langle E \rangle$ are mainly visible for small FRET efficiencies as measured in this work, when the values in the graphs are compared with those listed in the tables of PDA (see Supplementary Table Section). In order to address the questions about DNA binding/bending and MutS orientation, we investigated a set of four different DNA substrates with or without a mismatch at the central position (X_A:Y_D = [G_A:T_D, T_A:G_D, G_A:G_D, G_A:C_D,] see Figure 1A) both in the absence and presence of MutS (150 nM dimer).

The experimental smMFD results are displayed in a stack of 2D MFD-plots sharing the same *x*-axis (Figure 2A–E): (upper panels) apparent FRET

efficiency, $\langle E_a \rangle$, against the donor lifetime in the presence of acceptor, $\tau_{D(A)}$, and (lower panels) donor fluorescence anisotropy, r_D, against $\tau_{D(A)}$. The number of molecules (fluorescence bursts) in each bin are gray-scale coded from white (lowest) to black (highest). FRET efficiency $\langle E_a \rangle$, is determined from fluorescence intensity data of the donor and acceptor channels (see Supplementary Data Section 2.3) in an independent manner from the recovered lifetime of the donor, $\tau_{D(A)}$. A population of molecules with no FRET would appear as an 'island' close to $\langle E_a \rangle = 0$ and $\tau_{D(A)} = \tau_{D(0)}$, where $\tau_{D(0)}$ is the lifetime of the donor in the absence of the acceptor (in our case $\tau_{D(0)} = 3.8$ ns as determined from independent measurements). In Figure 2A–E, this population is denoted as Donor-only (D, green line). If FRET is present, correlated changes in $\langle E_a \rangle$ and $\tau_{D(A)}$ are expected, i.e. $\langle E_a \rangle$ should increase and $\tau_{D(A)}$ decrease according to the static FRET line $E_a = 1-(\tau_{D(A)}/\tau_{D(0)})$. This relation is illustrated by the red curve in the $\langle E_a \rangle$ versus $\tau_{D(A)}$ histograms. The $\langle E_a \rangle$ data are displayed in a logarithmic scale since all the FRET populations appeared to be relatively close to each other. This line provides a direct criterion for visual inspection of the results, since all FRET-related populations should follow this dependence. A deviation would indicate the existence of additional non-FRET related processes (photophysics, quenching, etc.) that can be responsible for erroneous interpretation of the FRET data if not taken into account. In our case, all measured FRET populations are located on the red curve which provides evidence that the recovered population differ in FRET. The combined 2D histograms of $\tau_{D(A)}$ versus r_D (Figure 2A–E, lower pannel) are valuable for the concurrent identification of specific anisotropies for the distinct FRET-species as well as contaminants.

In Figure 2A, we describe in detail the single-molecule results for free DNA as exemplified for the ds DNA G_A:T_D. The analysis of the MFD-plots in the first step reveals a major population around $\langle E_a \rangle \approx 0.1$ (denoted as LF, blue line), which is close to the predicted value $\langle E \rangle^{model} = 0.063$ for DNA alone. Thus, we assigned this population to unkinked free DNA. The mean donor anisotropy, r_D, for free DNA is 0.06 (monomodal distribution, blue histogram in the lower panel of Figure 2A), which corresponds to a mean rotational correlation time $\rho = 0.5$ ns (indicated by the lower red curve). This value suggests that the donor dye is almost unimpaired in its rotational freedom and it is appropriate to assume the value of 2/3 for κ^2 required to calculate distances from the observed $\langle E \rangle$-values via PDA (21). In the absence of MutS, all measurements of labeled DNAs containing different mismatches as well as a G:C homoduplex control revealed similar $\langle E_a \rangle$-distribution for the FRET populations, indicating that minor changes in structure/dynamics of the free DNA due to the presence of different mismatches are not detected. Detailed analysis of the $\langle E_a \rangle$-distribution with PDA in the second step shows that three populations are needed for a satisfactory fit (Figure 2F and Supplementary Table S1.7): LF, blue line, Donor-only (D, green line) and a third population we attributed to impurities (brown line). The major (and the only real FRET) population, LF, has a FRET average inter-dye $\langle R_{DA} \rangle_E = 82.3 \pm 1.3$ Å with the corresponding efficiency $\langle E \rangle = 0.070 \pm 0.007$ Å, which agrees well with the predicted value $\langle R_{DA} \rangle_E^{model} = 83.4$ Å ($\langle E \rangle^{model} = 0.063$) for unbent dsDNA. The standard deviation was obtained by analyzing the spread observed for all analyses done for this species within this work (see Supplementary Tables S1.4). Thus, we assigned this population to unkinked free DNA. It should be noted that the errors in the $<E>$ represent the standard deviation of the values obtained from independent measurements and they should be viewed in conjunction with the confidence intervals of the fitted parameters, as they are given in Supplementary Table S1.3. The second population, D, has a value for $\langle E_a \rangle \approx 0$, and a $\tau_{D(A)}$ of 3.8 ns that corresponds to the experimentally determined fluorescence lifetime of Alexa 488 in the absence of Alexa 594. Therefore, this population is DNA labeled with donor dye only (D, Donor-only, green line). It is observed in all samples. Finally, a minor population (3–10%) with a broad apparently HF distribution was observed and was assigned to impurities; note that this distribution was never populated to a significant extent and careful examination of 'bursts' arising from the buffer indicated that this minor population is due to a contaminant. The D and 'impurities' populations will not be further discussed in the subsequent text.

smMFD analysis of DNA–MutS complexes

The addition of MutS to the G_A:T_D substrate majorly shifted the FRET species in the $\langle E_a \rangle$ – $\tau_{D(A)}$ diagram of Figure 2B. The major population has a value close to $\langle E_a \rangle \approx 0.3$ and also a shorter donor fluorescence lifetime $\tau_{D(A)}$ of 2.5 ns so that it is denoted as HF (magenta line). PDA analysis (Figure 2G) revealed two FRET populations, HF ($\langle R_{DA} \rangle_E = 63.1 \pm 0.8$ Å ($\langle E \rangle = 0.265 \pm 0.013$)) and the already known LF species ($\langle R_{DA} \rangle_E = 82.3 \pm 1.3$ Å, ($\langle E \rangle = 0.070 \pm 0.007$)) corresponding to unkinked DNA (Figure 2A). Within the assumptions for creating the model of the G_A:T_D–MutS complex, the experimental FRET-averaged distance of the HF population agrees well with the predicted value of $\langle R_{DA} \rangle_E^{model} = 67$ Å and $\langle E \rangle^{model} = 0.20$. This result in solution is consistent with the findings of X-ray crystallography in Figure 1B that specifically bound MutS bends DNA at the mismatch by ~60°. Therefore, we assign the HF population to the specific G_A:T_D–MutS complex. The second species (LF) is fitted with a low $\langle E \rangle = 0.070 \pm 0.007$, which corresponds to unkinked DNA, as described earlier (Figure 2A). For the identification of the FRET populations in different measurements refer to the Supplementary Tables S1.4–S1.6, while for the confidence intervals of the fitted parameters refer to the Supplementary Tables S1.3 and S1.9.

The distribution of anisotropy is bimodal for both FRET species (Figure 2B, Lower panel): 76.7% of the distribution was fitted with a low r_D of 0.06 and 23.3% with a high r_D of around 0.2 (see upper red line in r_D versus $\tau_{D(A)}$ plot). Both LF and HF populations showed an r_D of 0.06, indicating the majority of donor fluorophores were still mobile as observed for G_A:T_D in the absence of MutS (Figure 2A). This result is consistent

with the absence of contact between MutS and the donor dye when the protein binds the mismatch with Phe-36 stacked on the T base in the lower strand (Figure 1C, Model II). The high r_D population will be addressed further below. We were interested in determining if the unkinked G_A:T_D DNA is free or MutS-bound, and thus measured the DNA diffusion times by subensemble Fluorescence Correlation Spectroscopy (seFCS) of bursts selected for this FRET species from the data trace (see Supplementary Data Section 2.4). The obtained apparent diffusion times are displayed in the bar diagrams of Figure 4A and B (left panel) for G_A:T_D DNA without and with MutS, respectively. The apparent diffusion times of both FRET species are clearly longer in the presence of MutS, which reveals that also unkinked DNA is in complex with MutS (Supplementary Figure S1). This population corresponds to either a non-specific DNA–MutS complex (MutS bound to any position on DNA) or to a specific unkinked DNA–MutS complex (MutS bound at the mismatch site but without inducing a kink). The latter species has been proposed earlier, based on AFM and FRET analysis of immobilized DNA (36,37); however, it remains to be shown if MutS is in direct contact with the mismatch in the unkinked complex, and whether this complex is a *bona fide* intermediate in the mismatch recognition pathway.

In summary, the smMFD analysis revealed at least three distinct DNA species for G_A:T_D in the presence of MutS, i.e. bound/unkinked DNA (LF/low r_D), bound/kinked (HF/low r_D) and a species with high r_D/broad distribution of donor lifetimes $\tau_{D(A)}$. Recent FRET analysis of *Thermus aquaticus* MutS binding to G:T mismatch also found two major FRET species (HF and LF) along with other species of intermediate FRET efficiencies (37).

Next, we tackled the specific question of directional MutS binding by analyzing two other DNA substrates: the switched substrate T_A:G_D, in which the mismatched bases are switched between the top and bottom strands relative to G_A:T_D (Figure 1), and the control substrate, G_A:G_D, containing a symmetric mismatch. If MutS binds mismatches with a preferred orientation, theoretically we can expect at least two different populations for the complexes with G:T, T:G and G:G DNAs:

(Scenario 1) High $\langle E_a \rangle$ and low r_D: If MutS stacks the conserved Phe on the mismatched base in the donor-labeled bottom strand, the DNA will be kinked such that the donor dye will not be close to the protein (G_A:$\underline{T}_D$, T_A:$\underline{G}_D$, G_A:$\underline{G}_D$, Figure 1C, Model II). A HF without an increase in r_D (low r_D) is expected in this case.

(Scenario 2) Low $\langle E_a \rangle$ and high r_D: If MutS stacks the conserved Phe on the mismatched base in the acceptor-labeled top strand, the DNA will again be kinked but in a way that the donor dye will be close to the protein ($\underline{G}_A$:T_D, $\underline{T}_A$:G_D, $\underline{G}_A$:G_D, Figure 1B, Model I). An increased r_D and possible quenching of donor fluorescence can be expected in this case.

So far, in the experiments with MutS and G_A:T_D described above, we detected majorly HF/low r_D species but less LF/high r_D species (Figure 2B and G), suggesting that in the absence of nucleotide, Phe stacks preferentially with T on the bottom strand in the G_A:T_D–MutS complex.

In the experiment with the switched DNA T_A:G_D, addition of MutS resulted in formation of a new FRET population with an $\langle E_a \rangle \approx 0.15$, which is in good agreement with the small FRET increase observed in the bulk measurement (Figure 1D). We refer to this population as Middle FRET (MF, Figure 2C and H orange line), which is the dominating FRET state as shown by PDA in Figure 2H. In contrast to the experiment with G_A:T_D and MutS, the HF population is absent. The MF population observed with T_A:G_D and MutS has a high donor anisotropy distribution with a mean r_D of 0.18 (mean rotational correlation time $\tau_{D(A)} = 2.8$ ns; upper red line in Figure 2C, Lower panel). With respect to the geometry description of the complex, we must note that the reduced mobility of the donor fluorophore, as indicated by the increase in r_D, makes distance estimations from $\langle E \rangle$ less reliable, since the orientation factor κ^2 may no longer be 2/3 (21). Importantly, the differences between the major populations obtained for G_A:T_D (HF/low r_D) and T_A:G_D (MF/high r_D) with MutS reflect differences in protein–dye interactions and, by implication, in MutS–mismatch interactions between these two DNA substrates. In accordance with the above predictions, the results indicate that MutS prefers to bind T_A:G_D in the opposite orientation as G_A:T_D, such that Phe is again stacked on the T base, now on the top strand. We can expect the effect of this biased interaction to be scrambled on a symmetric mismatch (due to MutS binding in both orientations), and we tested this prediction with the control substrate containing a G:G mismatch in the same sequence context as the G:T and T:G mismatches.

Addition of MutS to G_A:G_D results in broadened distributions of $\langle E_a \rangle$, $\tau_{D(A)}$ and r_D, which qualitatively resemble a mixture of the data obtained for G_A:T_D and T_A:G_D (Figure 2D). PDA analysis confirmed that a good fit could be obtained by assuming that both HF/low r_D (Phe stacked on Y, Model II in Figure 1) and MF/high r_D (Phe stacked on X, Model I in Figure 1) populations were present in the solution (Figure 2I). Thus, the data indicate that MutS binds a G:G mismatch in both orientations; however, on the asymmetric G:T (or T:G) mismatch, there is a preferred orientation in which the conserved Phe-X-Glu motif contacts the T base.

A final control experiment was performed with G_A:C_D homoduplex DNA. The MFD plots in Figure 2E confirm that the observed increase in $\langle E_a \rangle$ upon MutS binding to G_A:T_D, T_A:G_D and G_A:G_D DNAs was mismatch-specific since we did not observe an HF or MF population but rather a LF state with the G_A:C_D substrate (compare Figure 2A+F and 2E+J). In an earlier study, Wang *et al.* observed bent homoduplex DNA–MutS complexes by AFM imaging and suggested that they reflect MutS interacting with DNA in search of mismatch target sites (36). Our experimental setup was not designed to detect whether position independent (non-specific) DNA bending can be induced by MutS. The (seFCS) analysis showed an increased apparent diffusion time of the LF population as compared to DNA alone, confirming that under our experimental conditions the G_A:C_D

homoduplex DNA is bound to MutS (Supplementary Figure S1). Inspection of the donor anisotropy distribution revealed a minor fraction of increased r_D, indicating non-specific binding of MutS close to the donor fluorophore (Figure 2E). This non-specific binding explains the small population with high r_D observed with G_A:T_D (compare lower panel in Figure 2B and E), where MutS is bound near the dye instead of the mismatch.

In summary, smMFD analysis allowed us to discriminate between the two binding orientations of MutS revealing for the first time a strong bias in the way MutS homodimer interacts with a mismatched base in a solution. Qualitatively, the smMFD results confirmed the FRET efficiencies observed in bulk measurements (Figure 1D). Beyond that, the single molecule analysis provided an explanation for the different FRET efficiencies observed after MutS binding to DNA. We identified distinct populations corresponding to at least four different states of DNA–MutS interaction: (i) A mismatch-specific DNA–MutS complex observed with G_A:T_D and G_A:G_D with HF and low r_D in which the DNA is bent/kinked; the measured $\langle E_a \rangle$ is comparable to that calculated from the structural model (Figure 1). In this complex, MutS is bound with Phe-36 stacked on the bottom strand T or G of the G:T or G:G mismatch, respectively. (ii) A mismatch-specific DNA–MutS complex observed with T_A:G_D and G_A:G_D with middle FRET and high r_D. Contact between MutS and the donor fluorophore is likely responsible for the middle FRET signal. In this complex, MutS is bound with Phe-36 stacked on the top strand T or G of the T:G or G:T mismatch, respectively. (iii and iv) Two non-specific homoduplex DNA–MutS complexes (LF/low r_D and LF/high r_D).

Influence of nucleotides on G_A:T_D–MutS complexes observed in smMFD

Interactions of MutS with DNA during the search for mismatches, mismatch recognition and initiation of repair are modulated by its ATPase activity. In order to gain further insights into how nucleotides influence the structure and binding modes of DNA–MutS complex(es), we performed a series of smMFD measurements, either before or after addition of 1 mM ADP, ATP or the non-hydrolysable ATP analog AMP-PNP to the reaction containing MutS and G_A:T_D (Figure 3 and Supplementary Tables S1.8 and S1.9). To determine whether individual FRET populations contained unbound or MutS-bound DNA, apparent diffusion times of the complexes in the presence of the different nucleotides were also computed using subensemble FCS (Figure 4).

As shown above for G_A:T_D and MutS, in the absence of added nucleotide, two distinct FRET populations are observed in the MFD and PDA plots in Figures 3B and 4B, respectively: HF and LF with low r_D, and a smaller population with high r_D. Addition of 1 mM ADP resulted in an increase in the populations with HF efficiency and a decrease in the LF and the high r_D populations (Figures 3C and 4C, Supplementary Tables S1.8 and S1.9). A previous study using surface plasmon resonance had indicated that the specificity of MutS for mismatches is increased in the presence of ADP due to lowering of MutS affinity for homoduplex DNA (38). Our data showing a decrease in the non-specific DNA–MutS complex population agrees with that hypothesis. Following addition of 1 mM AMP-PNP to MutS and G_A:T_D only the LF population was observed (Figure 3D); there was no increase in r_D or in diffusion time for this species, which is as expected for free DNA (compare Figure 4A and D). The lack of DNA binding in the presence of non-hydrolysable AMP-PNP is consistent with the molecular switch model of MutS, i.e. that once ATP binds to MutS, ATP hydrolysis is required before the protein can interact with mismatched DNA again (39,40). Addition of 1 mM ATP to the reaction yielded similar results as ADP (Figures 3E and 4E), with PDA analysis showing the majority of DNA in the HF state. There were subtle differences in the occupancy of the LF versus MF region for ADP versus ATP, which may be explained by ongoing ATP hydrolysis resulting in a mixture of ATP-bound (primarily LF) and ADP-bound (primarily HF) species in the reaction with ATP. This hypothesis was tested by stopped-flow experiments as described below.

Stopped-flow ensemble FRET experiments

To measure the dynamics of the interaction and assess whether the behavior of the FRET species identified in smMFD is consistent with ensemble equilibrium and kinetic measurements, we performed complementary stopped-flow analysis of MutS binding to G_A:T_D DNA, using the change in FRET signal to monitor the complex (Figure 5A; donor excitation at 493 nm and acceptor emission at 610–685 nm). MutS was pre-incubated with ADP, ATP or AMP-PNP and mixed rapidly G_A:T_D DNA and the signal was monitored over a few seconds (Figure 5B). A fast rise in FRET was observed with ADP and ATP, but no change was observed in the presence of AMP-PNP. The binding data in the presence of ADP were fit empirically to a double-exponential function ($k_{obs1} = 11\,s^{-1}$ [amplitude A_1: 96.4%] and $k_{obs2} = 0.9\,s^{-1}$ [amplitude A_2 3.6%]). A bimolecular binding constant k_{on} of $4.4 \times 10^7\,M^{-1}\,s^{-1}$ (based on MutS concentration of 0.25 μM) can be estimated from the fast phase, which is similar to previously reported rates for MutS-DNA binding in a solution [e.g. $k_{on} = 3 \times 10^6\,M^{-1}\,s^{-1}$ for *T. aquaticus* MutS (40) and $k_{on} \sim 10^7\,M^{-1}\,s^{-1}$ for *S. cerevisiae* MutSα (41)]. In the presence of ATP, a three-exponential function was required to fit the binding curve; the initial fast increase in FRET was biphasic with similar rates as in the presence of ADP ($k_{obs1} = 17\,s^{-1}$ and $k_{obs2} = 1.9\,s^{-1}$), and was followed by a decrease in FRET signal ($k_{obs3} = 1.6\,s^{-1}$). The FRET increase is likely due to rapid association of nucleotide-free MutS with G_A:T_D, which is followed by ATP binding to G:T-bound MutS and its conversion to a sliding clamp form that releases the mismatched DNA, leading to a decrease in FRET. The steady state FRET

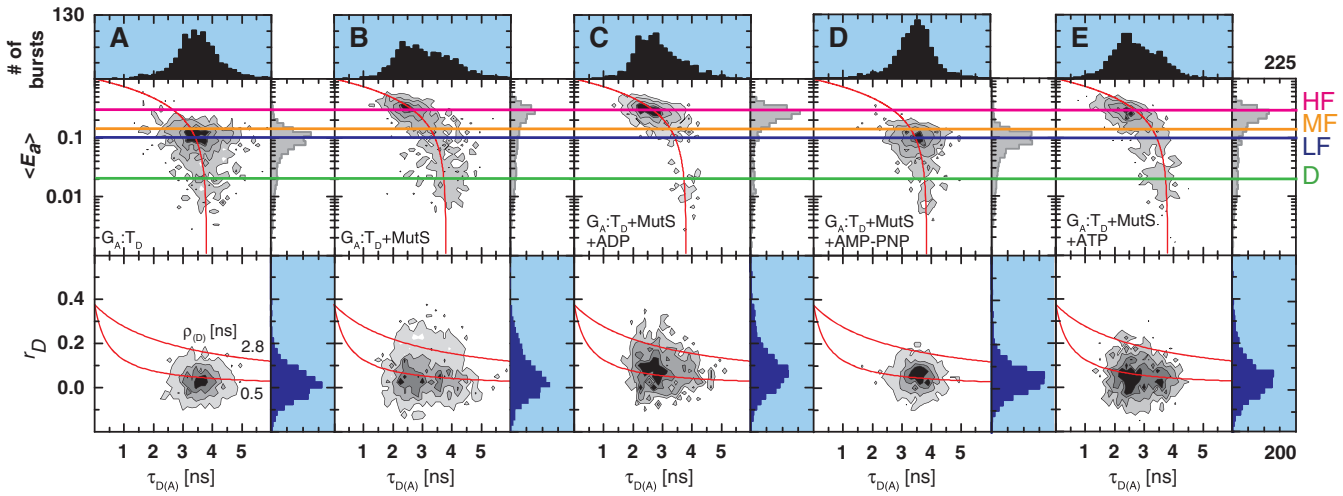

Figure 3. Nucleotides modulate the mismatch-binding properties of MutS. Two-dimensional fluorescence parameter histograms counting single-molecule bursts for smMFD measurements of free DNA (**A**) and MutS bound to G_A:T_D in the absence (**B**) and the presence of ADP (**C**), AMP-PNP (**D**) and ATP (**E**). In the MFD-plots, the number of molecules (fluorescence bursts) in each bin is gray-scale coded from white (lowest) to black (highest) and it is normalized to a total of 1000 bursts. Apparent FRET efficiency ($\langle E_a \rangle$, *Top*) and donor anisotropy (r_D, *Bottom*) are plotted versus $\tau_{D(A)}$. The same correction factors were used as in Figure 2. The population distributions indicate that ADP-bound MutS has less non-specific interactions (LF) with mismatched DNA and AMP-PNP-bound MutS cannot bind the G:T mismatch.

value observed in the presence of ATP is lower than in the presence of ADP. This finding is consistent with the smMFD data, which show a predominantly HF G_A:T_D–MutS population in the presence of ADP (Figure 4C), and an additional LF population in the presence of ATP but not ADP (Figure 4E). In the presence of AMP-PNP, MutS is likely in the closed conformation (clamp) that cannot bind mismatched DNA, thus no FRET increase is observed in both the stopped flow (Figure 5B) and smMFD experiments (Figures 3D and 4D).

We then investigated whether the HF G_A:T_D–MutS complex is a *bona fide* intermediate in the mismatch recognition pathway. It is well documented that when MutS is bound to a mismatch, it binds ATP rapidly and is stabilized in an ATP-bound conformation, which is required for signaling initiation of repair (42–44). Accordingly, we tested whether the HF G_A:T_D–MutS complex can undergo this ATP-induced switch in conformation. Stopped-flow experiments were performed in which pre-formed G_A:T_D–MutS complex was challenged with 1 mM ADP or ATP. ADP had virtually no effect on the FRET signal, which is consistent with smMFD data showing major HF species in the absence and presence of ADP (Figure 3). In contrast, adding ATP to the reaction resulted in biphasic kinetics, i.e. a fast decrease in FRET signal ($k_{obs1} = 2.3\,s^{-1}$) followed by an increase ($k_{obs2} = 1.4\,s^{-1}$). This result can be rationalized as follows: rapid ATP binding to G:T-bound MutS is followed by formation of an ATP-induced MutS sliding clamp that can slip off the ends of our linear DNA substrate (FRET decrease). Upon ATP-hydrolysis [k on the order of $1.4\,s^{-1}$ (45)], the resulting MutS–ADP complex can rebind DNA leading to an increase in FRET (45,46). This finding also explains the relatively minor differences in the smMFD results with ADP versus ATP, as the experiments were carried out under steady state conditions in which the ternary DNA–MutS–ATP complex is too short-lived to be detected.

In order to confirm that the second kinetic phase in the experiment with ATP corresponds to MutS re-binding the DNA, we challenged the pre-formed G_A:T_D–MutS complex with ADP or ATP in the presence of excess unlabeled G:T DNA trap (G:T-22, Figure 5D). The trap captures any free MutS and prevents its re-binding to the labeled DNA. Dissociation of MutS from the mismatch in the presence of ADP and G:T-22 is relatively slow ($k_{obs1} = 0.26\,s^{-1}$, 82% and $k_{obs2} = 0.08\,s^{-1}$, 18%) compared to dissociation in the presence of ATP ($k_{obs} = 1.9\,s^{-1}$). The rate constant for ATP-induced dissociation is comparable to the rate of the initial decrease in FRET observed in Figure 5C for the G_A:T_D–MutS complex challenged with ATP (in the absence of trap DNA) ($k_{obs1} = 2.3\,s^{-1}$). The absence of the subsequent increase in FRET in the trap experiment (Figure 5D) confirms that this second phase is due to MutS re-binding to the mismatched DNA. Note that the rate constants obtained from our stopped-flow experiments are about 10-fold faster than previous data obtained from surface plasmon resonance experiments (46). This order-of magnitude difference between in-solution versus surface-based experiments has been reported previously for MutS homologue Msh2/Msh6 (41). In the case of *E. coli* MutS, the difference may also be due to dimeric MutS (used in the present study) versus tetrameric MutS [used earlier; (46)]. In summary, the stopped flow FRET data complement the smMFD results, by showing that the HF G_A:T_D–MutS species is formed rapidly, and the fraction of HF and LF species is modulated by nucleotide binding to MutS, as expected for *bona fide* intermediates in the mismatch recognition and repair pathway.

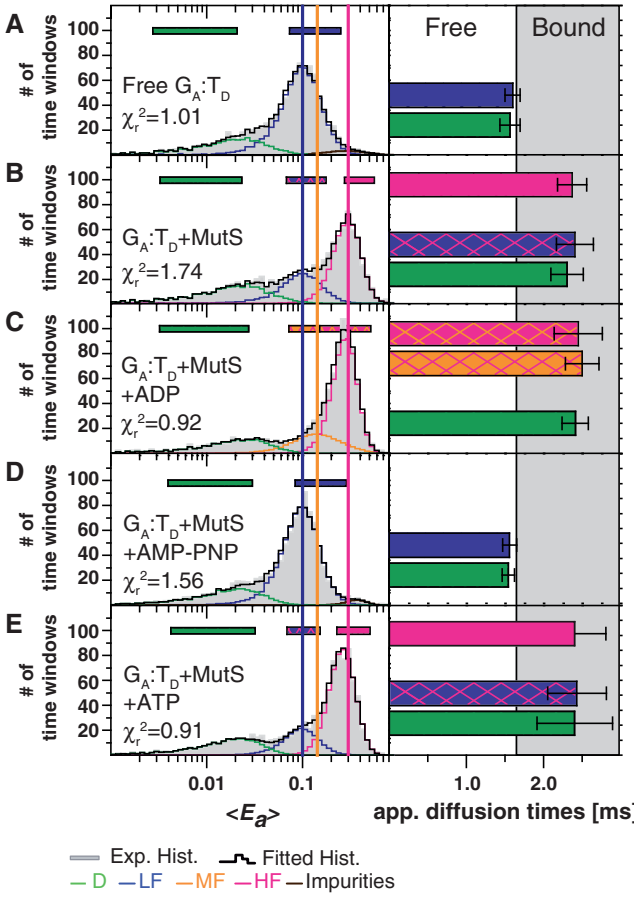

Figure 4. Subtle effects of nucleotides on DNA–MutS interaction parsed by PDA and sub-ensemble FCS analysis of the smMFD data. *Left*: PDA analysis of smMFD measurements of G_A:T_D in the absence (**A**) or the presence of MutS ± the indicated nucleotides. The PDA model functions of the fits were constituted by Gaussian distribution of inter-dye distances, with mean distance $\langle R_{DA}\rangle_E$, half-width HW and amplitude A (Supplementary Tables S1.2 and S1.8). (**B–E**) *Right*: Subensemble FCS analysis of the smMFD data yields apparent diffusion times for the various species (see Supplementary Data Section 2.4). The analyzed sub-populations are indicated by horizontal bars in the PDA plots—the two-colored bars indicate that the two species—LF/HF in (B) and (E) and MF/HF in (C)—were difficult to separate and diffusion time was calculated for the mixed population. In the bar histogram the white and gray regions indicate the range of diffusion times for free and bound DNA, respectively. The presence of an MF population in (B) is statistically justified (see Supplementary Figure S2).

Ensemble fluorescence anisotropy experiments reveal directional MutS binding to other asymmetric mismatches

The striking difference in donor fluorescence anisotropy between MutS-bound populations of G_A:T_D versus T_A:G_D detected in the smMFD analysis (Figure 2) suggested that steady-state fluorescence anisotropy of strategically located dyes on DNA could be a useful reporter of MutS-binding orientation on other asymmetric mismatches as well. We tested this possibility by monitoring the steady-state fluorescence anisotropy of both the donor (r_D) and acceptor (r_A) dyes in double- (X_A:Y_D) and single-labeled DNA substrates (X:Y_D or X_A:Y; Figure 6A and B) in the presence of ADP. Consistent with the smMFD data, only small changes in fluorescence anisotropy were detected for both donor (Δr_D) and the acceptor (Δr_A) dyes on the control homoduplex DNA (G_A:C_D) (Figure 6C). Furthermore, a large Δr_D value was obtained for T_A:G_D but not G_A:T_D (Figure 6C) again in agreement with the smMFD finding that MutS is in proximity to the donor dye when bound to T_A:G_D (Figure 2). Conversely, a large change in the acceptor fluorescence anisotropy (Δr_A) was observed with G_A:T_D but not with T_A:G_D (Figure 6C), indicating that MutS is in proximity to the acceptor dye when bound to G_A:T_D. These results are in agreement with MutS preferentially contacting the mismatched T in the top strand in T_A:G_D and the mismatched T in the bottom strand in G_A:T_D (Figure 1B and C). Once it was clear that ensemble fluorescence anisotropy is a reliable reporter of directional MutS binding to DNA, we investigated whether MutS exhibits a preferred binding orientation on a mismatch other than G:T (e.g. A:C/C:A). In order to do so, we tested single-labeled DNA substrates containing only a donor (X:Y_D) or an acceptor (X_A:Y) dye (Figure 6B); we also assessed possible sequence context effects by using DNA substrates in which the central sequence with the mismatch was inverted X:Y-I (Figure 6A). In the presence of MutS, a larger Δr_D relative to the homoduplex control (G:C_D) was observed only with T:G_D, A:C_D, (T:G_D)-I and to a lesser extent with G:G_D (Figure 6D). Conversely, a larger Δr_A relative to the homoduplex control (G_A:C) was observed only with G_A:T, C_A:A, G_A:G and (G_A:T)-I substrates (Figure 6E). Based on consistent findings from both smMFD and steady-state fluorescence anisotropy experiments, we can conclude that MutS binds G:T/T:G as well as C:A/A:C mismatches with a strong directional bias, such that the conserved Phe residue is stacked on the T base and A base of these mismatches, respectively. As is the case with crystal structures for G:T–MutS complexes (12,14,15), which all show MutS in contact with the T base, the crystal structure of the C:A–MutS complex shows MutS in contact with the A base (15), in agreement with our in solution results. Finally, experiments with MutS bound to a G:G mismatch revealed changes in both donor and acceptor fluorescence anisotropy (Figure 6D and E), consistent with smMFD results (Figure 2D and I), confirming lack of directional bias in MutS binding to a symmetric mismatch.

MutS orientation on DNA can influence initiation of MMR

The final question we asked in this study was whether the bias in MutS-binding orientation on mismatched DNA could possibly affect the directionality of MMR. In order to address this question, we first designed DNA substrates in which one binding orientation of MutS was deliberately disrupted. The footprint of MutS on a mismatch is asymmetric; thus, when MutS binds to a T:G mismatch in the preferred orientation, contacts are made to up to 5 bp on the 5′ side and 7 bp on the 3′ side of the T base. Consequently, placement of the T base less than 7 bp (6 bp) from the 3′ end of a linear DNA (T:G-6) should disrupt the binding interface for the

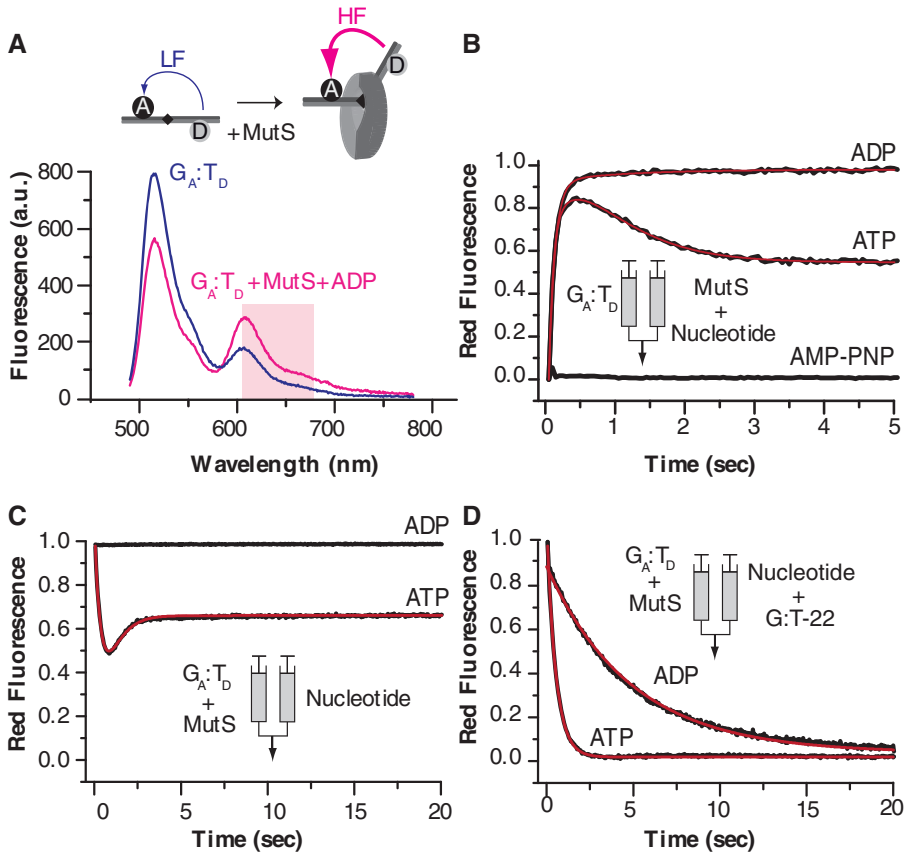

Figure 5. ATP binding induces fast dissociation of MutS from a mismatch, and weak re-association until ATP hydrolysis. (**A**) Steady state analysis of the interaction between G_A:T_D and MutS. Emission spectra of 42-bp DNA G_A:T_D in the absence (gray) or the presence of 250 nM MutS dimer and 1 mM ADP (black); the shaded area corresponds to the emission filter used in the stopped-flow experiments. (**B–D**) Pre-steady state analysis of G_A:T_D and MutS association (B) or dissociation (C, D) in the presence of different nucleotides using stopped-flow. Association kinetics were measured by mixing MutS (500 nM dimer), incubated with ADP (1 mM), ATP (1 mM) or AMP-PNP (2 mM), in 1:1 ratio with DNA (30 nM), and monitoring the FRET-sensitized red fluorescence over time. (C) The effect of ATP or ADP on the G_A:T_D–MutS complex was measured by mixing DNA (30 nM) incubated with MutS (500 nM dimer) in the 1:1 ratio with ADP or ATP (2 mM). (D) Dissociation kinetics were measured by challenging the pre-formed G_A:T_D–MutS complex with 75-fold molar excess of trap DNA (G:T-22) in the presence of ADP or ATP; the gray lines are the fits from sum of exponential functions to the data.

preferred MutS orientation and result in lower binding affinity (Figure 7 and Supplementary Figure S3). Conversely, for a G:T mismatch, placement of the G base 6 bp from the 3′ end (G:T-6) should have little effect on MutS binding in its preferred orientation, since more than 5 bp and 7 bp are available for interaction with the 5′ and 3′ sides of the mismatch, respectively. MutS binding to these 42 bp DNAs was compared with a positive control in which the mismatch was placed in the center of the DNA (T:G-22 and G:T-22) and a negative control of homoduplex DNA (G:C-22).

Competition titration experiments were performed to measure the affinity of MutS for the unlabeled DNA substrates described above (this test also allowed us to rule out any effects of dye molecules on MutS interaction with the mismatch). A pre-formed complex of G_A:T_D–MutS was challenged with increasing concentrations of the unlabeled substrates (G:T-22, G:T-6, T:G-22, T:G-6 or G:C-22, Supplementary Figure S3) and the change in FRET signal was monitored. The binding affinities of MutS for G:T-22, G:T-6 and T:G-22 were significantly higher relative to T:G-6, which was comparable with the homoduplex control G:C-22 (Figure 7B). The binding constant (K_A) for G:T-6 was only 1.3-fold lower than for G:T-22, whereas K_A for T:G-6 was 5-fold lower than for T:G-22, indicating that the preferred binding orientation of MutS is disrupted in T:G-6. Notably, the low affinity of MutS for T:G-6 cannot be explained by a substrate length or sequence context effect, supporting the hypothesis that MutS binds a mismatch with a preferred orientation.

Next, longer versions of the above substrates were used to assess whether MutS-binding orientation affects mismatched-provoked activation of MutH endonuclease by MutS and MutL *in vitro* by placing the mismatch close to the DNA ends thereby allowing binding in only one orientation (9). The 406 or 390 bp length DNAs contained a single unmethylated GATC-site 171 bp upstream of a mismatch, which was used to score MutH DNA cleavage activity. Five substrates (labeled with suffix L) were generated (Figure 7C), in which the mismatch-to-end distance was identical to the unlabeled short oligonucleotides used to measure MutS-binding affinity (Figure 7B). The results in Figure 7D show that DNA cleavage rates

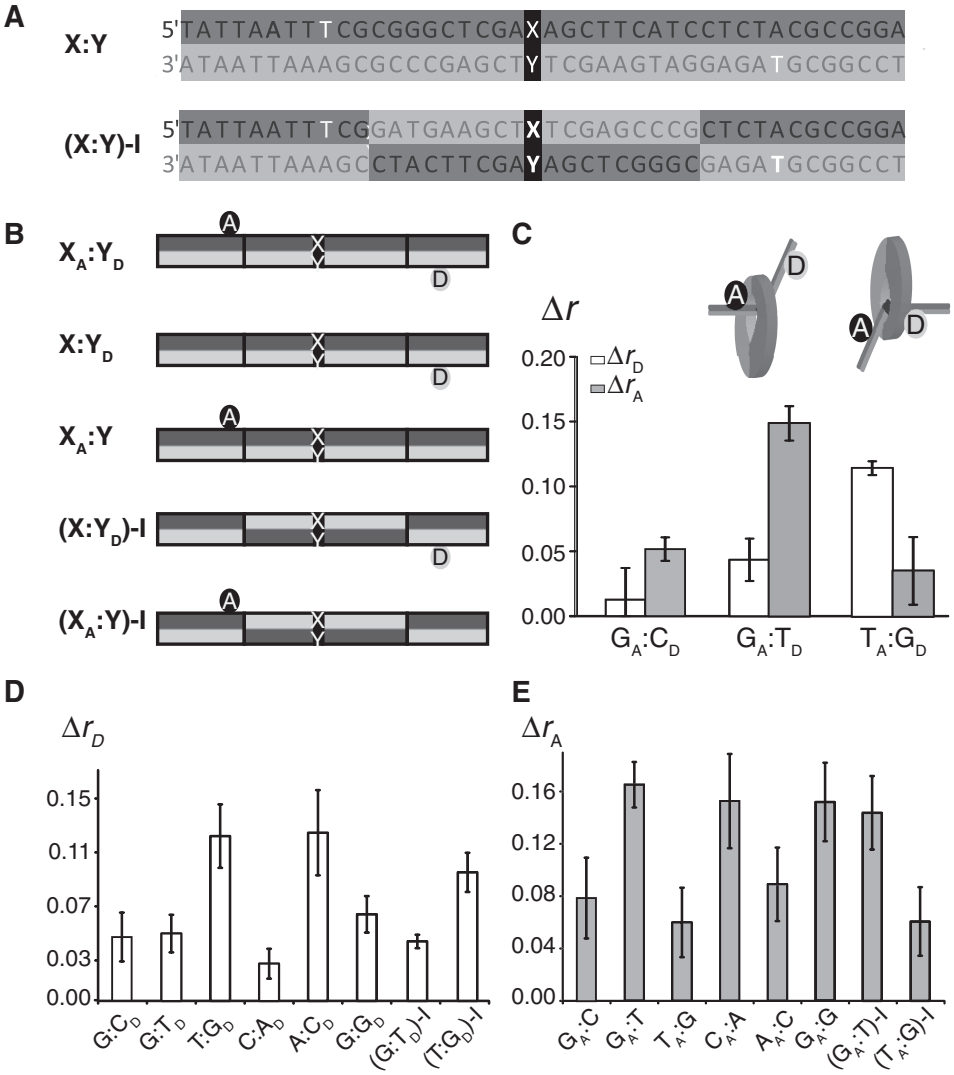

Figure 6. MutS-binding orientation is mismatch dependent, but sequence independent. Sequences (**A**) and schematic (**B**) of the labeled DNA substrates used in the experiments. The T bases labeled with acceptor (top strand) and the donor dye (bottom strand) shown in white. In the X:Y-I substrates, 9 bp flanking the X:Y base pair on both 5′ and 3′ sides are inverted. (**C–E**) Steady state fluorescence anisotropy of 42-bp DNA labeled with donor and/or acceptor dyes in the absence and the presence of MutS. (C) X_A:Y_D labeled-DNAs (10 nM), containing G:T, T:G or no mismatch (G:C) were incubated with MutS (125 nM dimer) and ADP (1 mM), and changes in fluorescence anisotropy (Δr) were measured for both the donor (Δr_D, white bars) and acceptor (Δr_A, gray bars) dyes (the error bars are standard deviations from at least three independent experiments). Changes in donor (D) and acceptor (E) fluorescence anisotropy of DNA labeled with either donor (X:Y_D or X:Y-I_D) or the acceptor dye (X:Y_D or X:Y-I_D) and the indicated mismatches (X:Y).

follow the same trend as DNA binding and, notably, the T:G-6-L was cleaved at a low rate comparable to that for the homoduplex control (G:C-22-L, Figure 7D). Thus, disruption of the preferred MutS-binding orientation on T:G-6-L results in poor initiation of MMR at this mismatch (i.e. forcing MutS to bind in the opposite orientation results in lower activation of MutH). In contrast, the three other substrates (G:T-22-L, G:T-6-L, T:G-22-L) showed significantly higher MutH cleavage activity than homoduplex DNA (Figure 7D). To summarize, the strong correlation between MutS DNA-binding and mismatch recognition-stimulated MutH endonuclease activities showed that the bias in MutS binding to asymmetric mismatches can translate into bias in repair efficiency.

CONCLUSIONS

In this study, we used smMFD and ensemble anisotropy studies in a solution to analyze binding of MutS to mismatched DNA. The results revealed at least two distinct DNA–MutS species with the DNA bent (in which MutS is positioned at the mismatch) and unbent/less bent (in which MutS is positioned at or away from the mismatch). Recent FRET DNA bending studies performed in the absence of nucleotide with immobilized dye-labeled DNA indicated multiple DNA–MutS complex states, which appear to undergo slow (on the timescale of our smMFD measurements) conformational transitions resulting in a broad distribution of bending angles (37). More significantly, our in-solution data

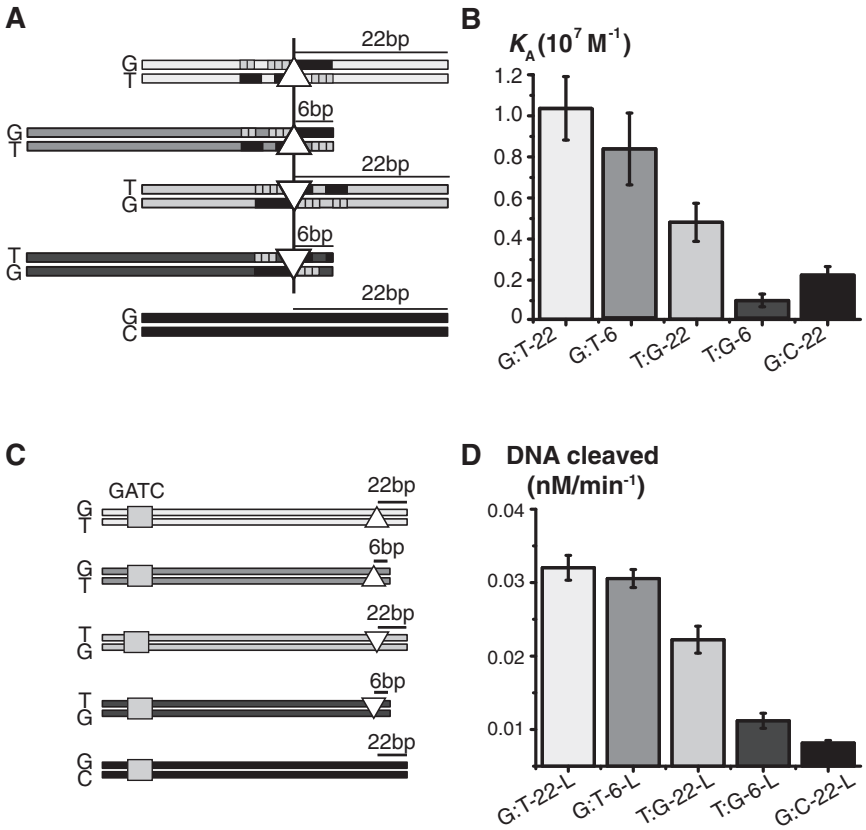

Figure 7. Initiation of MMR is affected by the MutS-binding orientation on DNA. (**A**) Schematic of the 42-bp DNA substrates used to compare MutS-binding affinity for unlabeled G:T and T:G mismatches, located 6 or 22 bp from the 3′ end. The shaded squares show bases contacted by mismatch-binding MutS subunit A (light gray) and non-mismatch-binding subunit B (dark gray) based on crystal structure [PDB code 1e3m (14)]. The black vertical line indicates the position of the mismatch and the triangles represent G:T (△) and T:G (▽). (**B**) MutS-binding affinity for the unlabeled DNA substrates shown in (A) was measured by competition experiments using G_A:T_D DNA [equilibrium binding constants (K_A) were determined by COPASI] (32). (**C**) Schematic of the long DNA substrates, containing a single unmethylated GATC site and the same mismatches and mismatch-end distances as in (A), used to test repair initiation in the mismatch-provoked MutH activation assay. (**D**) In the assay, the DNAs (15 nM) shown in (C) were reacted with MutS (250 nM), MutL (500 nM) and MutH (500 nM) over 0–60 minutes, and the DNA cleavage products were resolved by 6% PAGE to determine the rate of cleavage.

revealed that the MutS dimer binds asymmetric mismatches such as G:T or A:C in a preferred orientation, which explains the overwhelming bias in MutS orientation on DNA in crystal structures of these complexes (14,15). Recently published single-molecule data on the dynamics of lesion conformational changes induced by MutS homolog MSH2/MSH3 indicate that repair-resistant lesions are explained by different 'bending' dynamics (47). Similarly, the preferred MutS-binding orientation observed here might result from bending dynamics of asymmetric mismatches, where MutS can form a stable bent complex by stacking onto the T in the G:T and A in the A:C mismatches. We also demonstrated that this preferred binding orientation can influence the signaling capacity of MutS as monitored by mismatch-provoked activation of the strand discrimination endonuclease MutH (when MutS is blocked from binding a G:T mismatch in its preferred orientation, its interaction with DNA and activation of MutH is significantly reduced).

Our findings raise new questions for consideration in models of MutS function in mismatch recognition and signaling of DNA repair. According to several recent studies, MutS travels on DNA in search of mismatches (41,48,49), which implies that directional bias in mismatch recognition by MutS could result in a substantive fraction of mismatches left unnoticed within a single binding/scanning event (e.g. if the mismatch-binding subunit with the Phe-X-Glu motif is in contact with the G-containing strand for a G:T mismatch). This may not be a problem in the case of homodimeric MutS proteins, as the two subunits may switch mismatch-binding function while bound to DNA although such a phenomenon has not been demonstrated thus far and would have to involve switching of ATP binding/hydrolysis functions as well. In the case of eukaryotic heterodimeric MutS proteins, like human MSH2/MSH6, switching of mismatch-binding sites is not an option since only MSH6 has the conserved Phe-X-Glu motif (12,50,51); although we have not examined heterodimeric MutS proteins in this study, there is one report indicating directional binding of *S. cerevisiae* Msh2/Msh6 on a G:T mismatch (17). One possible solution to the problem posed by directional mismatch recognition is release/rebinding of MutS and eventual coverage of all mismatch

orientations in multiple rounds of MutS scanning DNA. Another possibility is that the MutL dimer overcomes directional mismatch recognition by symmetric interaction with the MutS dimer; although again, in the case of eukaryotes, the MutS–MutL complex has intrinsic asymmetry, as only the MLH1 subunit of the MLH1/PMS2 MutL homolog is known to bind MSH2/MSH6 (52), and thus far only MSH2 is known to have an interaction site for MLH1/PMS2 (53). However, even if the MutS–MutL interaction is asymmetric, MutL subunits have highly flexible linker regions between their MutS- and MutH-binding domains (or endonuclease domain, in the case of MutH independent MMR), which may re-introduce symmetry into the system. The same effect is possible if the connection between proteins at the mismatch site and the endonuclease site occur through space, by DNA looping. Finally, it is also possible that interaction between repair proteins (e.g. MutS and MutL) and replication proteins (e.g. circular clamps: *E. coli* β, human PCNA) can impose the correct orientation for signaling repair of the newly-synthesized error-containing strand (54). It is likely that one or more of these mechanisms (or yet other alternatives) is in play during MMR, as *in vivo* and *in vitro* studies of the *E. coli* system indicate that repair of the error-containing strand occurs with similar efficiency irrespective of the relative orientation of the mismatched bases and the hemimethylated GATC site (4,55–58). It remains to be shown exactly how the bias in mismatch recognition introduced by MutS is scrambled, such that ultimately all mismatches are repaired effectively irrespective of their orientation on the two strands of DNA.

SUPPLEMENTARY DATA

Supplementary Data are available at NAR Online: Supplementary Tables 1.1–1.9, Supplementary Figures 1–3, Supplementary Methods and Supplementary References [59–68].

ACKNOWLEDGMENTS

The authors are grateful to Joyce Lebbink and Humberto Sanchez for critically reading the manuscript and to Stanislav Kalinin for FRET modeling.

FUNDING

The European Community's Sixth Framework Program (FP6/2004–2006) under grant agreements No. MOBILITY-1 19566 (to P.F., M.C., P.R. and C.S.); The European Community's Seventh Framework Program (FP7/2007–2013) under grant agreements No. HEALTH-F4-2008-223545 to P.F. and the German Science Foundation (GRK 1384/1). Funding for open access charge: DFG (Deutsche Forschungsgemeinschaft) and the University of Giessen.

Conflict of interest statement. None declared.

REFERENCES

1. Modrich,P. and Lahue,R. (1996) Mismatch repair in replication fidelity, genetic recombination, and cancer biology. *Annu. Rev. Biochem.*, **65**, 101–133.
2. Iyer,R.R., Pluciennik,A., Burdett,V. and Modrich,P.L. (2006) DNA mismatch repair: functions and mechanisms. *Chem. Rev.*, **106**, 302–323.
3. Kunkel,T.A. and Erie,D.A. (2005) DNA Mismatch Repair. *Annu. Rev. Biochem.*, **74**, 681–710.
4. Lahue,R.S., Au,K.G. and Modrich,P. (1989) DNA mismatch correction in a defined system. *Science*, **245**, 160–164.
5. Fishel,R. and Kolodner,R.D. (1995) Identification of mismatch repair genes and their role in the development of cancer. *Curr. Opin. Genet. Dev.*, **5**, 382–395.
6. Peltomaki,P. and Vasen,H.F. (1997) Mutations predisposing to hereditary nonpolyposis colorectal cancer: database and results of a collaborative study. The International Collaborative Group on Hereditary Nonpolyposis Colorectal Cancer. *Gastroenterology*, **113**, 1146–1158.
7. Bjornson,K.P., Blackwell,L.J., Sage,H., Baitinger,C., Allen,D. and Modrich,P. (2003) Assembly and molecular activities of the MutS tetramer. *J. Biol. Chem.*, **278**, 34667–34673.
8. Lamers,M.H., Georgijevic,D., Lebbink,J.H., Winterwerp,H.H., Agianian,B., de Wind,N. and Sixma,T.K. (2004) ATP increases the affinity between MutS ATPase domains. Implications for ATP hydrolysis and conformational changes. *J. Biol. Chem.*, **279**, 43879–43885.
9. Manelyte,L., Urbanke,C., Giron-Monzon,L. and Friedhoff,P. (2006) Structural and functional analysis of the MutS C-terminal tetramerization domain. *Nucleic Acids Res.*, **34**, 5270–5279.
10. Mendillo,M.L., Putnam,C.D. and Kolodner,R.D. (2007) Escherichia coli MutS tetramerization domain structure reveals that stable dimers but not tetramers are essential for DNA mismatch repair in vivo. *J. Biol. Chem.*, **282**, 16345–16354.
11. Drummond,J.T., Li,G.M., Longley,M.J. and Modrich,P. (1995) Isolation of an hMSH2-p160 heterodimer that restores DNA mismatch repair to tumor cells. *Science*, **268**, 1909–1912.
12. Warren,J.J., Pohlhaus,T.J., Changela,A., Iyer,R.R., Modrich,P.L. and Beese,L.S. (2007) Structure of the human MutSalpha DNA lesion recognition complex. *Mol. Cell*, **26**, 579–592.
13. Tseng,Q., Orans,J., Hast,M.A., Iyer,R.R., Changela,A., Modrich,P.L. and Beese,L.S. (2011) Purification, crystallization and preliminary X-ray diffraction analysis of the human mismatch repair protein MutSbeta. *Acta Crystallogr. Sect. F Struct. Biol. Cryst. Commun.*, **67**, 947–952.
14. Lamers,M.H., Perrakis,A., Enzlin,J.H., Winterwerp,H.H., de Wind,N. and Sixma,T.K. (2000) The crystal structure of DNA mismatch repair protein MutS binding to a G x T mismatch. *Nature*, **407**, 711–717.
15. Natrajan,G., Lamers,M.H., Enzlin,J.H., Winterwerp,H.H., Perrakis,A. and Sixma,T.K. (2003) Structures of Escherichia coli DNA mismatch repair enzyme MutS in complex with different mismatches: a common recognition mode for diverse substrates. *Nucleic Acids Res.*, **31**, 4814–4821.
16. Obmolova,G., Ban,C., Hsieh,P. and Yang,W. (2000) Crystal structures of mismatch repair protein MutS and its complex with a substrate DNA. *Nature*, **407**, 703–710.
17. Jiang,J., Bai,L., Surtees,J.A., Gemici,Z., Wang,M.D. and Alani,E. (2005) Detection of high-affinity and sliding clamp modes for MSH2-MSH6 by single-molecule unzipping force analysis. *Mol. Cell*, **20**, 771–781.
18. Rothwell,P.J., Berger,S., Kensch,O., Felekyan,S., Antonik,M., Wöhrl,B.M., Restle,T., Goody,R.S. and Seidel,C.A.M. (2003) Multiparameter single-molecule fluorescence spectroscopy reveals heterogeneity of HIV-1 reverse transcriptase:primer/template complexes. *Proc. Natl Acad. Sci. USA*, **100**, 1655–1660.
19. Widengren,J., Kudryavtsev,V., Antonik,M., Berger,S., Gerken,M. and Seidel,C.A. (2006) Single-molecule detection and identification of multiple species by multiparameter fluorescence detection. *Anal. Chem.*, **78**, 2039–2050.
20. Kalinin,S., Felekyan,S., Valeri,A. and Seidel,C.A. (2008) Characterizing multiple molecular states in single-molecule

multiparameter fluorescence detection by probability distribution analysis. *J. Phys. Chem. B*, **112**, 8361–8374.
21. Wozniak,A.K., Schröder,G.F., Grubmüller,H., Seidel,C.A. and Oesterhelt,F. (2008) Single-molecule FRET measures bends and kinks in DNA. *Proc. Natl Acad. Sci. USA*, **105**, 18337–18342.
22. Sisamakis,E., Valeri,A., Kalinin,S., Rothwell,P.J. and Seidel,C.A. (2010) Accurate single-molecule FRET studies using multiparameter fluorescence detection. *Methods Enzymol.*, **475**, 455–514.
23. Feng,G. and Winkler,M.E. (1995) Single-step purifications of His_6-MutH, His_6-MutL and His_6-MutS repair proteins of *Escherichia coli* K-12. *BioTechniques*, **19**, 956–965.
24. Giron-Monzon,L., Manelyte,L., Ahrends,R., Kirsch,D., Spengler,B. and Friedhoff,P. (2004) Mapping protein-protein interactions between MutL and MutH by cross-linking. *J. Biol. Chem.*, **279**, 49338–49345.
25. Toedt,G.H., Krishnan,R. and Friedhoff,P. (2003) Site-specific protein modification to identify the MutL interface of MutH. *Nucleic Acids Res.*, **31**, 819–825.
26. van Dijk,M. and Bonvin,A.M. (2009) 3D-DART: a DNA structure modelling server. *Nucleic Acids Res.*, **37**, W235–W239.
27. Dlakic,M. and Harrington,R.E. (1998) DIAMOD: display and modeling of DNA bending. *Bioinformatics*, **14**, 326–331.
28. Sindbert,S., Kalinin,S., Nguyen,H., Kienzler,A., Clima,L., Bannwarth,W., Appel,B., Müller,S. and Seidel,C.A. (2011) Accurate distance determination of nucleic acids via Forster resonance energy transfer: implications of dye linker length and rigidity. *J. Am. Chem. Soc.*, **133**, 2463–2480.
29. Selvin,P.R. (1995) Fluorescence resonance energy transfer. *Methods Enzymol.*, **246**, 300–334.
30. Antonik,M., Felekyan,S., Gaiduk,A. and Seidel,C.A. (2006) Separating structural heterogeneities from stochastic variations in fluorescence resonance energy transfer distributions via photon distribution analysis. *J. Phys. Chem. B*, **110**, 6970–6978.
31. Kalinin,S., Felekyan,S., Antonik,M. and Seidel,C.A. (2007) Probability distribution analysis of single-molecule fluorescence anisotropy and resonance energy transfer. *J. Phys. Chem. B*, **111**, 10253–10262.
32. Hoops,S., Sahle,S., Gauges,R., Lee,C., Pahle,J., Simus,N., Singhal,M., Xu,L., Mendes,P. and Kummer,U. (2006) COPASI—a COmplex PAthway SImulator. *Bioinformatics*, **22**, 3067–3074.
33. Thomas,E., Pingoud,A. and Friedhoff,P. (2002) An efficient method for the preparation of long heteroduplex DNA as substrate for mismatch repair by the Escherichia coli MutHLS system. *Biol. Chem.*, **383**, 1459–1462.
34. Gansen,A., Valeri,A., Hauger,F., Felekyan,S., Kalinin,S., Tóth,K., Langowski,J. and Seidel,C.A. (2009) Nucleosome disassembly intermediates characterized by single-molecule FRET. *Proc. Natl Acad. Sci. USA.*, **106**, 15308–15313.
35. Jiang,Y. and Marszalek,P.E. (2011) Atomic force microscopy captures MutS tetramers initiating DNA mismatch repair. *EMBO J.*, **30**, 2881–2893.
36. Wang,H., Yang,Y., Schofield,M.J., Du,C., Fridman,Y., Lee,S.D., Larson,E.D., Drummond,J.T., Alani,E., Hsieh,P. *et al.* (2003) DNA bending and unbending by MutS govern mismatch recognition and specificity. *Proc. Natl Acad. Sci. USA*, **100**, 14822–14827.
37. Sass,L.E., Lanyi,C., Weninger,K. and Erie,D.A. (2010) Single-molecule FRET TACKLE reveals highly dynamic mismatched DNA-MutS complexes. *Biochemistry*, **49**, 3174–3190.
38. Blackwell,L.J., Bjornson,K.P., Allen,D.J. and Modrich,P. (2001) Distinct MutS DNA-binding modes that are differentially modulated by ATP binding and hydrolysis. *J. Biol. Chem.*, **276**, 34339–34347.
39. Gradia,S., Acharya,S. and Fishel,R. (1997) The human mismatch recognition complex hMSH2-hMSH6 functions as a novel molecular switch. *Cell*, **91**, 995–1005.
40. Jacobs-Palmer,E. and Hingorani,M.M. (2007) The effects of nucleotides on MutS-DNA binding kinetics clarify the role of MutS ATPase activity in mismatch repair. *J. Mol. Biol.*, **366**, 1087–1098.
41. Zhai,J. and Hingorani,M.M. (2010) Saccharomyces cerevisiae Msh2-Msh6 DNA binding kinetics reveal a mechanism of targeting sites for DNA mismatch repair. *Proc. Natl Acad. Sci. USA*, **107**, 680–685.
42. Antony,E. and Hingorani,M.M. (2003) Mismatch recognition-coupled stabilization of Msh2-Msh6 in an ATP-bound state at the initiation of DNA repair. *Biochemistry*, **42**, 7682–7693.
43. Antony,E. and Hingorani,M.M. (2004) Asymmetric ATP binding and hydrolysis activity of the thermus aquaticus MutS dimer is key to modulation of its interactions with mismatched DNA. *Biochemistry*, **43**, 13115–13128.
44. Gradia,S., Subramanian,D., Wilson,T., Acharya,S., Makhov,A., Griffith,J. and Fishel,R. (1999) hMSH2-hMSH6 forms a hydrolysis-independent sliding clamp on mismatched DNA. *Mol. Cell*, **3**, 255–261.
45. Bjornson,K.P., Allen,D.J. and Modrich,P. (2000) Modulation of MutS ATP hydrolysis by DNA cofactors. *Biochemistry*, **39**, 3176–3183.
46. Lebbink,J.H., Fish,A., Reumer,A., Natrajan,G., Winterwerp,H.H. and Sixma,T.K. (2010) Magnesium coordination controls the molecular switch function of DNA mismatch repair protein MutS. *J. Biol. Chem.*, **285**, 13131–13141.
47. Lang,W.H., Coats,J.E., Majka,J., Hura,G.L., Lin,Y., Rasnik,I. and McMurray,C.T. (2011) Conformational trapping of mismatch recognition complex MSH2/MSH3 on repair-resistant DNA loops. *Proc. Natl Acad. Sci. USA*, **108**, E837–E844.
48. Jeong,C., Cho,W.K., Song,K.M., Cook,C., Yoon,T.Y., Ban,C., Fishel,R. and Lee,J.B. (2011) MutS switches between two fundamentally distinct clamps during mismatch repair. *Nat. Struct. Mol. Biol.*, **18**, 379–385.
49. Gorman,J., Chowdhury,A., Surtees,J.A., Shimada,J., Reichman,D.R., Alani,E. and Greene,E.C. (2007) Dynamic basis for one-dimensional DNA scanning by the mismatch repair complex Msh2-Msh6. *Mol. Cell*, **28**, 359–370.
50. Bowers,J., Sokolsky,T., Quach,T. and Alani,E. (1999) A mutation in the MSH6 subunit of the Saccharomyces cerevisiae MSH2-MSH6 complex disrupts mismatch recognition. *J. Biol. Chem.*, **274**, 16115–16125.
51. Dufner,P., Marra,G., Räschle,M. and Jiricny,J. (2000) Mismatch recognition and DNA-dependent stimulation of the ATPase activity of hMutSalpha is abolished by a single mutation in the hMSH6 subunit. *J. Biol. Chem.*, **275**, 36550–36555.
52. Plotz,G., Welsch,C., Giron-Monzon,L., Friedhoff,P., Albrecht,M., Piiper,A., Biondi,R.M., Lengauer,T., Zeuzem,S. and Raedle,J. (2006) Mutations in the MutSalpha interaction interface of MLH1 can abolish DNA mismatch repair. *Nucleic Acids Res.*, **34**, 6574–6586.
53. Mendillo,M.L., Hargreaves,V.V., Jamison,J.W., Mo,A.O., Li,S., Putnam,C.D., Woods,V.L. Jr and Kolodner,R.D. (2009) A conserved MutS homolog connector domain interface interacts with MutL homologs. *Proc. Natl Acad. Sci. USA*, **106**, 22223–22228.
54. Hombauer,H., Srivatsan,A., Putnam,C.D. and Kolodner,R.D. (2011) Mismatch repair, but not heteroduplex rejection, is temporally coupled to DNA replication. *Science*, **334**, 1713–1716.
55. Au,K.G., Welsh,K. and Modrich,P. (1992) Initiation of methyl-directed mismatch repair. *J. Biol. Chem.*, **267**, 12142–12148.
56. Grilley,M., Griffith,J. and Modrich,P. (1993) Bidirectional excision in methyl-directed mismatch repair. *J. Biol. Chem.*, **268**, 11830–11837.
57. Bruni,R., Martin,D. and Jiricny,J. (1988) d(GATC) sequences influence Escherichia coli mismatch repair in a distance-dependent manner from positions both upstream and downstream of the mismatch. *Nucleic Acids Res.*, **16**, 4875–4890.
58. Cooper,D.L., Lahue,R.S. and Modrich,P. (1993) Methyl-directed mismatch repair is bidirectional. *J. Biol. Chem.*, **268**, 11823–11829.
59. Eggeling,C., Berger,S., Brand,L., Fries,J.R., Schaffer,J., Volkmer,A. and Seidel,C.A. (2001) Data registration and selective single-molecule analysis using multi-parameter fluorescence detection. *J. Biotechnol.*, **86**, 163–180.
60. Eggeling,C., Widengren,J., Brand,L., Schaffer,J., Felekyan,S. and Seidel,C.A. (2006) Analysis of photobleaching in single-molecule

multicolor excitation and Förster resonance energy transfer measurements. *J. Phys. Chem. A*, **110**, 2979–2995.
61. Clegg,R.M. (1992) Fluorescence resonance energy transfer and nucleic acids. *Meth. Enzymol.*, **211**, 353–388.
62. Eggeling,C., Schaffer,J., Seidel,C.A.M., Korte,J., Brehm,G., Schneider,S. and Schrof,W. (2001) Homogeneity, transport, and signal properties of single Ag particles studied by single-molecule surface-enhanced resonance Raman scattering. *J. Phys. Chem. A*, **105**, 3673–3679.
63. Lakowicz,J.R. (2006) *Principles of Fluorescence Spectroscopy*, 3rd edn. Springer, New York.
64. Koshioka,M., Sasaki,K. and Masuhara,H. (1995) Time-dependent fluorescence depolarization analysis in 3-dimensional microspectroscopy. *Appl. Spectr.*, **49**, 224–228.
65. Torella,J.P., Holden,S.J., Santoso,Y., Hohlbein,J. and Kapanidis,A.N. (2011) Identifying molecular dynamics in single-molecule FRET experiments with burst variance analysis. *Biophys. J.*, **100**, 1568–1577.
66. Philip,B.R. and Robinson,D.K. (2002) *Data Reduction and Error Analysis for the Physical Sciences*. McGraw Hill, New York.
67. Ehrenberg,M. and Rigler,R. (1974) Rotational brownian motion and fluorescence intensify fluctuations. *Chem. Phys.*, **4**, 390–401.
68. Magde,D., Elson,E. and Webb,W.W. (1972) Thermodynamic fluctuations in a reacting system: measurement by fluorescence correlation spectroscopy. *Phys. Rev. Lett.*, **29**, 705.

Supplementary Data

1 Supplementary Materials and Methods

1.1 Single-molecule spectroscopy

Single molecule measurements of a very dilute solution (~15 pM) of double-labeled DNA molecules were performed with a confocal epi-illuminated microscope. The donor fluorophore (Alexa 488) was excited by a linearly polarized, active-mode-locked Argon-ion laser (476.5 nm, 73 MHz, 300 ps). The laser light is focused into the solution with a 60x/1.2 water immersion objective. Fluorescence bursts arising by single molecules diffusing through the detection volume are detected. This photon-train is divided initially into its parallel and perpendicular components via a polarizing beamsplitter and then into wavelength ranges below and above 595 nm. Additionally, red (HQ 630/66 nm) and green (HQ 533/46 nm) filters in front of the detectors ensure that only photons emitted by the acceptor (Alexa 594) and donor (Alexa 488) molecules are registered. The focal geometry is estimated from the measured diffusion correlation time (200 ± 13 µs) and the known diffusion coefficient (0.34 ± 0.03 μm^2/ms) for Rhodamine 110. In addition, correction factors l_1 = 0.0308 and l_2 = 0.0368 are used to account for the mixing of polarization by the microscope objective, and a factor G = 1.02 is applied to compensate for the slightly different detection efficiency of the two polarization components. Detection is performed using four avalanche photodiodes (SPCM-AQR-14, Laser Componen ts, Germany). The signals from all detectors are passed through a passive delay unit and two routers to two synchronized time-correlated single photon counting boards (SPC 132, Becker and Hickl, Germany) that are connected to a PC. Fluorescence bursts are distinguished from the background of 1-3 kHz by applying a threshold intensity criterion (~0.05 ms interphoton time, 100 photons minimum per burst).

1.2 Modeling the 42bp G:T heteroduplex DNA

A 3D structure of the unbent DNA was obtained by introducing the sequence into the 3D-DART webserver (26). A model of the MutS-bound kinked DNA was obtained by using the DNA

distortion parameters obtained from the NDB server (ndbserver.rutgers.edu) using the crystal structure of MutS and DNA (PDB code 1e3m). Parameters of positions 2-16 from chain E (15-29 from chain F) were used for position 14-28 (57-71) of the 42bp G:T-DNA or positions 57-71 (14-28) for the T:G DNA, respectively, while using B-DNA parameters (obtained from the 3D-DART webserver using the same sequence) for all other positions. Sequence-dependent structural bending of the chosen DNA sequence is not significant as judged by the program DIAMOD (27).) MutS was docked to this modeled DNA by superposition of the backbone atoms of the DNA in the co-crystal structure onto the respective atoms of the modeled DNA using the Swiss PDB viewer (version 4.07).

1.3 Modeling the fluorophore position cloud obtained from MD simulations to the MutS-DNA complex structure.

We used accessible volume (AV) simulations to describe the rotational freedom of the fluorophore dependent on the linker length and steric clashes with the DNA (28). For each calculation of a position distribution, we used the real physical dimensions of the fluorophore and performed three independent AV simulations with three different radii $R_{dye(i)}$ and superimposed them. Thus, the obtained position distribution represents an average weighted by the number of allowed positions. Throughout this work we used for Alexa488 $R_{dye(1)}$ = 5 Å, $R_{dye(2)}$ = 4.5 Å and $R_{dye(3)}$ = 1.5 Å and for Alexa594 $R_{dye(1)}$ = 6.7 Å, $R_{dye(2)}$ = 4.5 Å and $R_{dye(3)}$ = 1.5 Å. It turned out that these “mixed” AV simulations are necessary to accurately predict dye distributions. In these simulation the length l and the width w of dyes linkers was the same for both dyes (l = 20 Å, w = 4.5 Å). The theoretical distance between the fluorophores was measured between the center of mass of the fluorophores’ accessible space. A Förster distance (R_0) of 53.2 Å was used to calculate the transfer efficiency *E*. For free B-DNA$_{DA}$ the theoretical distance was calculated from the mean position of the fluorophores to be R_{mp} 85 Å (E_{mp} of 0.063).

2 Supporting theory for FRET analysis

2.1 Burst selection

As discrete molecules are diffusing through the detection volume, bursts of fluorescence photons are registered in the detected photon trace. These bursts are selected against background as

described in (58). In this study, additional burst selection steps were performed on the fluorescent bursts recovered from smMFD measurements, in order to reduce the background (FRET-inactive species) and allow the analysis to be constrained to the FRET-active subpopulations. Two selection steps were performed:

a) $-0.45<T_g-T_r<0.45$: Here the bursts during which an event of acceptor photobleaching occurs were excluded. The time difference T_g-T_r of the mean observation time of all photons detected for the donor and acceptor channels within a single molecule fluorescence burst enables identification and exclusion of photobleached molecules (59). T_g and T_r represent the medial time of fluorescence emission of both detection channels. Without photobleaching, T_g and T_r would be similar and thus $T_g-T_r \approx 0$.

b) $N_{ph,RED}>20$: Bursts with less than 20 photons in the red channel, $N_{ph,RED}$, were excluded from the analysis. This step enables exclusion of small red bursts that are not originated by FRET, but either by direct excitation of the acceptor or by crosstalk from green donor signal into the red acceptor detection channel. In this way, a significant fraction of the donor-only species was removed from the analysis.

The performed burst selection does not change the position or the widths of the FRET populations, and can be thus used to significantly reduce the background and facilitate the analysis.

2.2 Calculation of FRET and fluorescence anisotropy parameters

The efficiency, *E*, of FRET depends strongly on the interdye distance R_{DA} and the Förster radius, R_0 (Equation 1).

$$E = \left[1+\left(\frac{R_{DA}}{R_0}\right)^{1/6}\right]^{-1} \qquad (\textit{Equation 1})$$

Each fluorophore pair has a characteristic Förster radius, R_0, which accounts for the photophysical properties and relative orientation of the dyes. It is calculated (in Å) by

$$R_0 = \left(c_{FT}\, J(\lambda)\, \kappa^2\, \Phi_{FD(0)}\, n^{-4}\right)^{(1/6)} \qquad (\textit{Equation 2})$$

where $J(\lambda)$ is the overlap integral of the donor emission with the acceptor absorption spectrum (M^{-1} cm^{-1} nm^4), κ^2 accounts for the relative orientation of the donor and acceptor (usually assumed to be 2/3), $\Phi_{FD(0)}$ is the donor fluorescence quantum yield in absence of transfer (0.6 for Alexa 488 attached to DNA), and n is the refractive index of the medium (n=1.33). For the given units the constant c_{FT} equals 8.79 10^{-5} mol.

For MFD-plots the efficiency of energy transfer is calculated from a number of different parameters, including the fluorescence intensities of the donor or acceptor (F_D or F_A), donor lifetime ($\tau_{D(A)}$) in the presence of acceptor, and from the anisotropy (r) of either the donor or the acceptor fluorophore (29,60). We determine the efficiency of the energy transfer using the fluorescence intensity ratio between the donor and acceptor (F_D/F_A) (18). For analysis of these data the signal intensities (S_G and S_R) were corrected for background counts (typically 1.5-3.0 kHz for the green channels, B_G (donor), and 0.5-1.5 kHz for the red channels, B_R (acceptor)), spectral crosstalk, α (0.058), and the ratio of the detection efficiencies, g, between the green and red channels (g_G/g_R = 0.78) (Equation 3).

$$F_D = \frac{S_G - B_G}{g_G} = \frac{F_G}{g_G}$$
$$F_A = \frac{(S_R - B_R) - \alpha(S_G - B_G)}{g_R} = \frac{F_R}{g_R} \qquad (\textit{Equation 3})$$

For the specific dye pair used in this study, a small fraction of the recorded counts in the acceptor channel are due to direct excitation of the acceptor by the incoming laser light (let these counts be denoted as DE). In PDA an accurate determination of the FRET efficiency requires taking this effect into account. Thus equation 3 should be rewritten as follows:

$$F_A = \frac{S_R - (\langle B_R \rangle + DE) - \alpha(S_G - \langle B_G \rangle)}{g_R} = \frac{F_R}{g_R} \qquad (\textit{Equation 4})$$

If direct excitation is not considered, we refer to the FRET efficiency E as apparent FRET efficiency E_a. If the quantum yield of the acceptor, Φ_{FA}, is taken into account (0.9 as measured for Alexa 594 attached to DNA), the efficiency of the energy transfer, *E*, can be calculated as:

$$E = \frac{\frac{F_A}{\Phi_{FA}}}{\frac{F_A}{\Phi_{FA}} + \frac{F_A}{\Phi_{FD(0)}}} \qquad (\textit{Equation 5})$$

It is important to note, that in MFD-plots the apparent FRET efficiency $\langle E_a \rangle$ is computed without correcting for direct acceptor excitation so that the apparent FRET efficiencies in MFD-plots are slightly higher than the FRET efficiencies $\langle E \rangle$ obtained by PDA, where the correction for direct excitation is implemented. The differences between E_a and E are mainly visible for small FRET efficiencies as measured in this work.

By combining Equation 1 and Equation 5 the analysis of the interdye distance can be performed by the help of the following equation:

$$R_{DA} = R_0 \left(\frac{\Phi_{FA}}{\Phi_{FD(0)}} \frac{F_D}{F_A} \right)^{1/6} \qquad (\textit{Equation 6})$$

For the data analysis by equation 1 and 5 we experimentally determined the Förster radius (R_0 =53.2 Å), for the Alexa 488-Alexa 594 pair.

The fluorescence lifetime is determined for each burst in two steps: (i) by generating a histogram of photon arrival times, and (ii) by fitting the histograms to a single exponential using a maximum likelihood estimator and iterative convolutions to account for the scatter contribution (61). The lifetime of the donor molecule in the absence of the acceptor ($\tau_{D(0)}$) was determined to be 3.8 ns. The efficiency of energy transfer is related to fluorescence lifetimes through (Equation 5):

$$E = 1 - \frac{\tau_{D(A)}}{\tau_{D(0)}} \qquad (\textit{Equation 7})$$

where $\tau_{D(A)}$, $\tau_{D(0)}$ is the lifetime of the donor in the presence and in absence of the acceptor respectively.

Another useful parameter calculated for each burst is the steady-state polarization anisotropy (62-63) of the donor, r_D. This value is determined by using Equation 8:

$$r_D = \frac{gS_{//} - S_{\perp}}{(1-3l_2)gS_{//} + (2-3l_1)S_{\perp}} \qquad \textit{(Equation 8)}$$

The ratio of the detection efficiencies of the detection of the parallel and the perpendicular polarized photons is given as *g*. The factors l_1 and l_2 account for polarization mixing because of the objective as described (63). The anisotropy is linked to the donor lifetime via Perrin's equation:

$$r_D = r_0\left(\frac{\tau_{D(A)}}{\rho_D} + 1\right)^{-1} \qquad (\textit{Equation 9})$$

In Equation 7, ρ_D is the rotational correlation time of D and r_0 is the fundamental anisotropy. Strictly speaking, the Perrin equation is valid only if the anisotropy decay is single-exponential, which is usually not the case. Still, the rotational correlation time in Equation 7 qualitatively reflects the rotational mobility of the dye, which is the collective result of the rotation of the dye molecule itself and the overall rotation of the biomolecule to which the dye is attached. In a 2-D plot of r_D vs $\tau_{D(A)}$ the theoretical relation described in Perrin's equation can be illustrated as a curve (Perrin curve) and an estimation of the mobility can be obtained.

2.3 Photon Distribution Analysis (PDA)

Photon distribution analysis (PDA) calculates the theoretical probability of recording a particular combination of red and green photons for a given FRET efficiency, and thus distance, can be derived from this analysis (19). PDA quantitatively describes the shapes of FRET distributions measured by MFD, including the effect of background and shot-noise in the distribution. Both the mean and width of a distribution are the functions of the mean FRET efficiency (31). With the PDA approach, a single parameter, which corresponds to the mean FRET efficiency, determines automatically the maximum width and asymmetry of the distribution that can be

assigned to shot-noise. Any additional broadening is attributed to the real interdye distance distribution, which can reveal biologically relevant heterogeneities in an ensemble of biomolecules (19).

2.3.1 Fitting

Each individual burst was divided into time windows of 2ms and histograms of the recovered FRET efficiencies for each time window were created by using Equations 3, 4 and 5. By inspection of the histograms for various time windows one could identify the presence of any dynamic processes occurring in the ~ms time scale. In the current study both PDA analysis with varying time windows and also FCS data revealed no dynamic behavior in the ~ms range.

General information about the fitting procedure of FRET efficiency distributions with PDA is presented below, followed by specific details about the fits used in this study. The choice of the form of the model function is crucial when fitting the data, since multiple FRET-efficiency states are commonly observed in the experimental histograms. That is the fitting procedure proceeds in conjunction with testing of alternative hypotheses regarding the model function (22,64). In the procedure it is important that the number of free parameters used in each fit is minimized by exploiting additional measurements (i.e. measurements of Donor only).

The experimental histograms in this study were fitted using in-house developed software. The model functions in all cases were given in interdye distances, $\langle R_{DA} \rangle_E$. A small percentage of direct excitation of the acceptor (p_{DE}=3.5% as determined in (34) was also taken into account during the fitting procedure).

For all measurements it was statistically justified to use a model function containing 3 states for achieving a good fit (see SI Fig.1 and main text Fig 2-4).These populations accounted for Donor only (D_{only}, green line in the main text figures 2 and 4), one or two of the FRET-states (LF, MF, HF) and in the measurements, for which no HF was present, impurities (dark brown line). In all measurements there was a population of D_{only}, which has very low $\langle E \rangle$, accounts for around 20-50% of the total number of recorded bursts and it could be fitted by a single FRET apparent distance ($\langle R_{DA} \rangle_E$ =110 Å as was determined by independent measurements and fixed for all fits).

For all measurements, a Gaussian distribution of interdye distances was used for each of the other two fitted states present in the model function (determined by mean value: $\langle R_{DA} \rangle_E$ and halfwidth: HW). In measurements of G_A:T_D (main text Figure 2F), T_A:G_D +MutS(main text Figure 2F), G_A:C_D +MutS (main text Figure 2J) the majority of the population belongs to one FRET state (either LF or MF) and the third state accounts for a small fraction of impurities. The population due to impurities varied between 3-10 % and exhibited a broad FRET distribution with $\langle R_{DA} \rangle_E$ close to the HF population as determined by independent measurement. Please note that this distribution was never populated to a significant extent and careful examination of "bursts" arising from the buffer indicated that this minor population is indeed arising from impurities in the preparation of the buffer. In the cases in which HF population was present the impurities could not be retrieved because they overlap with the strongly populated HF state. In principle only the shoulder of impurity populations is visible in the PDA histogram, because its peak is hidden in the presence of the HF population. Thus in the cases G_A:T_D +MutS (main text Figure 2G), G_A:G_D +MutS (main text Figure 2I) the fitting function, apart from D_{only}, respectively included HF and LF in the former case and HF and MF in the latter. All the above comments could be summarized and referred to what we will note as:

***Fitmodel 1*:** Initially only the Donor-only population was fixed and the other two states were left free to vary (3 free parameters per Gaussian distribution: mean distance $\langle R_{DA} \rangle_E$, Half width HW, Amplitude (A). For all measurements the fitting procedure was successful with low χ_r^2-values as it is shown in Supplementary Tables S1.1-1.3. Some concerns arose only for the cases of G_A:T_D-MutS-ATP and G_A:T_D-MutS-ADP, since in these cases the fits were unstable regarding the low FRET population as illustrated by the large confidence intervals retrieved for these populations.

The results by using ***Fitmodel 1*** are presented in tables (see tables S1.1- S1.6). In tables S1.1-S1.2 the model function for each measurement is presented together with the corresponding χ_r^2. In the table S1.3 one could evaluate the stability of the fits of some representative measurements by inspecting the 68% confidence intervals of all parameters. Moreover the identification of the individual FRET relevant states LF, MF and HF could be judged by inspecting tables S1.4- 1.6. One could observe small variations for the mean distance and HW of each state. The identified states LF, MF and HF are well discriminated as demonstrated by the values of the mean distances and the corresponding values of the FRET efficiencies (LF: $\langle R_{DA} \rangle_E$ = 82.3 ±1.3 Å,

$\langle E \rangle$ = 0.070 ± 0.007, MF: $\langle R_{DA} \rangle_E$ = 73.2 ± 3.1 Å , $\langle E \rangle$ = 0.17 ± 0.04, HF: $\langle R_{DA} \rangle_E$ = 63.1 ± 0.8 Å , $\langle E \rangle$ = 0.27 ± 0.01).

An argument could be made that FRET state 1 in the case of G_A:T_D-MutS-ADP is different than in the case of T_A:G_D-MutS (see Supplementary Table S1.1-2 and S1.5). These states are indeed different as proven by analysis of additional fluorescence parameters like donor anisotropy (see main text section "smMFD analysis of DNA-MutS complexes"), which is high in the T:G-MutS MF population but not in the G_A:T_D-MutS-ADP MF population (Figure 2 and Figure 5 in the main text and). Nevertheless, in order to describe PDA histograms with a minimal number of states following the parsimony principle, no additional states were included; thus the middle FRET population for G_A:T_D-MutS-ADP and T_A:G_D-MutS were considered to be identical for the purpose of data fitting. The HF population for G_A:T_D, G_A:T_D-MutS-ADP and G_A:T_D-MutS-ATP has $\langle R_{DA} \rangle_E$ values of 62.3 Å, 64.2 Å and 63.2 Å. Since the differences in R_{mean} are small and all values of $\langle R_{DA} \rangle_E$ lie within the confidence intervals of each other (Figure S1), we have chosen to consider these states as one. As an alternative, we preferred a fitmodel (which yielded equally good fits as shown in Supplement Table 1.9), where the relevant FRET states, were identified from the measurements in which they were predominant and only their relative fractions were left to vary.

This fitmodel which we will denote as **Fitmodel 2** could be described as follows:

Fitmodel 2:The FRET state LF ($\langle R_{DA} \rangle_E$ = 82.7 Å, HW = 7.1 Å) was determined by taking the average values for $\langle R_{DA} \rangle_E$ and HW of the distributions obtained in the measurements of free DNAs (G_A:T_D , G_A:G_D, G_A:C_D , T_A:G_D)). HF and MF were fixed to the values retrieved for the corresponding measurements of G_A:T_D+MutS and T_A:G_D+MutS (HF: $\langle R_{DA} \rangle_E$ = 62.3 Å, HW = 4.1 Å and MF: $\langle R_{DA} \rangle_E$ = 75 Å, HW = 9.3 Å). Only the relative fractions of these states were left to vary in each fit. The HF population was always consisted of a narrow distribution (HW~ 4 Å) as a result in the cases of G_A:T_D, G_A:T_D-MutS-ADP and G_A:T_D-MutS-ATP has $\langle R_{DA} \rangle_E$ values of 62.3 Å, 64.2 Å and 63.2 Å were used since when using the fixed value of HF the χ_r^2 got significantly worse. Nevertheless, by inspecting table S.1.6 it is clear that all these high FRET distributions describe the same state (the variation in the mean distance value is only 0.8 Å).

The results of the fits with Fitmodel 2 are more robust (compare table S1.9 and table S1.3), yielding more restricted confidence intervals with comparable $\chi_{\mathbf{r}}^2$-values as compared to the fits with Fitmodel 1. Thus, all results presented in the main text are from Fitmodel 2. All the results of fits with both Fitmodel 1 and 2 are presented in the supplement tables S1.1- S1.9, in order to illustrate that fixing the states does not alter qualitatively the results of the fits. Although 5 states are needed to describe all data for all different measurements, the number of free parameters per fit is limited as the D_{only} peak is identified from independent measurements and because the fitting function for a single data set includes only 2 states, in addition to the fixed states for the D_{only} population and the impurity population (6 free parameters per fit as shown in Supplementary Table S1.1 to S1.3 for Fitmodel 1 and 2-4 free parameters per experiment as shown in Supplementary Table S1.7-S1.9 for Fitmodel 2).

2.3.2 Error limits for multiple parameters

All free parameters of each fit were varied in a random manner around their optimal values. The $\chi_{\mathbf{r}}^2$-value was calculated at 30000-55000 random points yielding more than 100 fits with $\chi_{\mathbf{r}}^2$-values within $\pm (2/N_{bins})^{1/2}$ of the $\chi_{\mathbf{r}}^2$-value of the optimal fit (the degrees of freedom of the fit were N_{bins} = 55-59) (65). Parameter intervals within these fits were assigned as confidence intervals, as presented in Supplementary Tables for some typical measurements.

2.4 Subensemble Fluorescence Correlation Spectroscopy (seFCS)

FCS is based on analysis of the fluctuations in fluorescence intensity (66-67). The origin of the fluctuations is not critical for the technique, thus FCS offers a unique tool for the direct study of phenomena like diffusion and photophysics and, via these phenomena, for the study of biologically relevant processes including macromolecular interactions (from the Stokes-Einstein relation it follows than the bigger a molecule the slower its diffusion in solution). Binding of the labeled oligonucleotides to MutS was investigated by FCS in this study, since unbound oligonucleotides diffuse faster than MutS-bound ones. seFCS curves were produced only for a specific subensemble by correlating signals from the green parallel and the green perpendicular detection channel of selected bursts, corresponding to individual FRET-states subpopulations as described in (61). Each correlation curve was fitted to a model function $G(t_{lag})$ with the lag (correlation) time t_{lag} (see equation 10) including 2 bunching terms in the 1-300 μs scale

accounting for the photophysics of the donor dye (triplet state kinetics , with a characteristic time of ~5 μs and a minor additional term around 250 μs which is assigned to dynamic fluorescence quenching). It should be noted that the data registration scheme utilized for smMFD enables use of the same data sets for correlation analysis as well as analysis of specific subpopulations of molecules. The diffusion times of the various FRET subpopulations were determined and compared in order to assess the free versus bound states of the molecules. The formula of the model function used is given below:

$$G\left(t_{lag}\right)=1+\frac{1}{N}\cdot\frac{1}{1+\frac{t_{lag}}{t_d}}\cdot\frac{1}{\sqrt{1+\frac{t_{lag}}{\omega^2 t_d}}}\cdot\left(1-T_1+T_1\cdot e^{-\frac{t_{lag}}{t_{T1}}}-T_2+T_2\cdot e^{-\frac{t_{lag}}{t_{T2}}}\right) \qquad \text{(}\textit{Equation 10}\text{)}$$

,where N is the total number of molecules present in the detection volume, t_d is the apparent diffusion correlation time (slightly distorted by the burst cutting procedure), ω is the geometrical parameter of the detection volume (66-67). T_1 , T_2 are the amplitudes and t_{T1}, t_{T2} the corresponding characteristic times of the two bunching terms.

Supplementary Table 1.1: **Various mismatches.** Fitting results for which the FRET populations are left free to vary **(Fitmodel 1)**. LF: Blue background, MF: Orange background, HF: Magenta background, D_{only}: Light green background, Impurities: Dark brown background.

System	Model function											χ_r^2
	State 1					State 2					D_{only}	
	$\langle R_{DA}\rangle_E$ [1] [Å]	HW [2] [Å]	A [3]	Rel. A [4] [%]	$\langle E\rangle$ [6]	$\langle R_{DA}\rangle_E$ [1] [Å]	HW [2] [Å]	A [3]	Rel. A [%]	$\langle E\rangle$ [6]	A_{fixed} [5]	
G_A:T_D	82.2	7.0	67.7	96.9	0.068	59.5	5.7	2.2	3.1	0.34	30.1	1.0
G_A:T_D-MutS	79.5	13.3	31.8	46.2	**0.082**	62.30	4.1	37.1	53.8	**0.28**	31.1	**1.2**
T_A:G_D	82.3	6.6	42.6	93.0	**0.068**	60.9	9.0	3.2	7.0	**0.31**	54.2	**0.75**
T_A:G_D-MutS	75	9.3	68.8	98.4	**0.11**	49.9	1.8	1.1	1.6	**0.60**	30.1	**1.5**
G_A:G_D	83.5	7.6	39.3	98.5	**0.063**	56	7.2	0.6	1.5	**0.42**	60.1	**1.1**
G_A:G_D-MutS	75.1	11.4	43.1	67.3	**0.11**	63.2	3.3	20.9	32.7	**0.26**	36	**1.1**
G_A:C_D	82.7	7.2	59.1	91.3	**0.066**	74.3	18.3	5.6	8.7	**0.12**	35.3	**0.94**
G_A:C_D-MutS	83.3	7.9	65.7	94.0	**0.064**	63.7	9.4	4.2	6.0	**0.25**	30.1	**0.84**

[1] $\langle R_{DA}\rangle_E$ corresponds to the FRET-averaged distance between the dyes , [2] **HW** to the half width of the distribution (see Supplementary Section 2.3.1).[3] **A** refers to the amplitude of a given population as given by the fit, [4] **rel. A** refers to the relative amplitude of the population in relation only to the FRET populations (Donor-only excluded). [5] $\mathbf{A_{fixed}}$ refers to the Donor-only population, considered fixed at 110Å, [6] $\langle E\rangle$ corresponds to the FRET efficiency value for Förster radius of 53.2 Å and an interdye distance $\langle R_{DA}\rangle_E$.

Supplementary Table 1.2: **Nucleotide Effect**. Results of fits for which the FRET populations are left free to vary **(Fitmodel 1)**. LF: Blue background, MF: Orange background, HF: Magenta background, D_{only}: Light green background, Impurities: Dark brown background.

System	Model function											χ_r^2
	State 1					State 2					D_{only}	
	$\langle R_{DA}\rangle_E$ [1] [Å]	HW[2] [Å]	A[3]	Rel. A[4] [%]	$\langle E\rangle$ [6]	$\langle R_{DA}\rangle_E$ [1] [Å]	HW[2] [Å]	A[3]	Rel. A[4] [%]	$\langle E\rangle$ [6]	A_{fixed}[5]	
G_A:T_D	82.2	7.0	67.7	96.9	**0.068**	59.5	5.7	2.2	3.1	**0.34**	30.1	1
G_A:T_D- MutS	79.5	13.3	31.8	46.2	**0.082**	62.3	4.1	37.1	53.8	**0.28**	31.1	1.23
G_A:T_D-MutS-AMP-PNP	82.4	6.1	69.1	95.8	**0.068**	60.7	4.5	3	4.2	**0.31**	27.9	1.51
G_A:T_D- MutS-ATP	80.2	12.1	25.3	33.9	**0.079**	64.1	4.2	49.4	66.1	**0.25**	25.3	0.79
G_A:T_D- MutS-ADP	69.6	9.2	32.1	43.5	**0.17**	62.8	2.5	41.7	56.5	**0.27**	26.2	0.8

[1]$\langle R_{DA}\rangle_E$ corresponds to the FRET-averaged distance between the dyes, [2]**HW** to the half width of the distribution (see Supplementary Section 2.3.1).[3]**A** refers to the amplitude of a given population as given by the fit, [4]**rel. A** refers to the relative amplitude of the population in relation only to the FRET populations (D_{only} excluded). [5]$\mathbf{A_{fixed}}$ refers to the donor-only population, considered fixed at 110Å, [6]$\langle E\rangle$ corresponds to the FRET efficiency value for Förster radius of 53.2 Å and an interdye distance $\langle R_{DA}\rangle_E$.

Supplementary Table 1.3: Nucleotide Effect. Results of fits for which the FRET populations are left free to vary (Fitmodel 1). In black the 95% confidence intervals are given for each parameter. In the parenthesis in red the value of each parameter corresponding to the best fit is given for direct comparison. The columns of the mean distance and the corresponding mean FRET efficiency are shown in bold. The confidence intervals were calculated as described in Supplementary Section 2.3.2. Similar confidence intervals were obtained for the measurements not described in this table. LF: Blue background, MF: Orange background, HF: Magenta background, D_{only}: Light green background, Impurities: Dark brown background.

System	Model Function (Only Gaussian Distributions)								χ_r^2
	State 1				State 2				
	$\langle R_{DA} \rangle_E$ [1] [Å]	HW [2] [Å]	Rel. A [3] [%]	$\langle E \rangle$ [4]	$\langle R_{DA} \rangle_E$ [1] [Å]	HW [2] [Å]	Rel. A [3] [%]	$\langle E \rangle$ [4]	
G_A:T_D	**81.1-83.5** (82.2)	5.8-7.8 (6.8)	92.5-98.1 (95.7)	**0.06-0.07** (0.07)	**55.0-69.3** (61.7)	4.8-8.9 (6.9)	1.9-7.5 (4.3)	**0.17-0.45** (0.29)	0.91-1.29
G_A:T_D-MutS	**75.7-85.4** (79.5)	9.8-16.2 (13.2)	35.5-54.3 (46.1)	**0.06-0.10** (0.08)	**61.4-63.3** (62.3)	3.3-4.9 (4.1)	45.7-64.5 (53.9)	**0.26-0.3** (0.28)	1.13-1.52
T_A:G_D-MutS	**74.2-76.0** (75.1)	8.5-10.6 (9.3)	96.9-100 (98.5)	**0.11-0.12** (0.11)	**41.3-59.8** (50.0)	0.4-3.7 (2.1)	0.0-3.1 (1.5)	**0.33-0.82** (0.60)	1.36-1.75
G_A:T_D-MutS-ADP	**67.0-73.7** (69.6)	7.2-11.6 (9.2)	29.3-56.4 (43.5)	**0.12-0.20** (0.17)	**62-63.5** (62.8)	2.1-2.8 (2.5)	43.6-70.7 (56.5)	**0.26-0.29** (0.27)	0.74-1.13
G_A:T_D-MutS-ATP	**74.6-88.1** (80.2)	8.4-15.7 (12.1)	19.8-50.1 (33.8)	**0.05-0.12** (0.08)	**63.1-65.2** (64.1)	3.4-5.1 (4.2)	49.9-80.2 (66.2)	**0.23-0.26** (0.25)	0.72-1.11

[1] $\langle R_{DA} \rangle_E$ corresponds to the FRET-averaged distance between the dyes, [2] **HW** to the half width of the distribution (see Supplementary Section 2.3.1). [3] **rel. A** refers to the relative amplitude of the population in relation only to the FRET populations (D_{only} excluded). [4] $\langle E \rangle$ corresponds to the FRET efficiency value for Förster radius of 53.2 Å and an interdye distance $\langle R_{DA} \rangle_E$.

Supplementary Table 1.4: **Identification of LF state from Fitmodel 1.**

System	Low FRET state (LF)	
	$\langle E \rangle$	$\langle R_{DA} \rangle_E$ [Å]
G:C	0.066	82.7
G:C+MutS	0.064	83.3
G:T	0.068	82.2
G:T+MutS	0.082	79.5
T:G	0.068	82.3
G:G	0.063	83.5
G:T+MutS+AMPnP	0.068	82.4
G:T+MutS+ATP	0.079	80.2
Mean value	0.070	82.3
Standard deviation	0.007	1.3

Supplementary Table 1.5: **Identification of MF state from Fitmodel 1.**

System	**Middle FRET state (MF)**	
	$\langle E \rangle$	$\langle R_{DA} \rangle_E$ [Å]
T:G+MutS	0.11	75
G:T+MutS+ADP	0.17	69.6
G:G+MutS	0.1	75.1
Mean value	0.127	73.2
Standard deviation	0.038	3.1

Supplementary Table 1.6 Identification of HF state from Fitmodel 1.

System	**HighFRET state (HF)**	
	$\langle E \rangle$	$\langle R_{DA} \rangle_E$ [Å]
G:T+MutS	0.28	62.3
G:T+MutS+ATP	0.25	64.1
G:T+MutS+ADP	0.27	62.8
G:G+MutS	0.26	63.2
Mean value	0.265	63.1
Standard deviation	0.013	0.8

Supplementary Table 1.7: **Different mismatches**. Results of fits for which the FRET populations were fixed (Fitmodel 2) as described in the text (Supplementary Section 2.3.1). LF: Blue background, MF: Orange background, HF: Magenta background, D_{only}: Light green background, Impurities: Dark brown background.

System	Model function											χ_r^2
	State 1					State 2					D_{only}	
	$\langle R_{DA} \rangle_E$ [1] [Å]	HW [2] [Å]	A [3]	Rel. A [4] [%]	$\langle E \rangle$ [6]	$\langle R_{DA} \rangle_E$ [1] [Å]	HW [2] [Å]	A [3]	Rel. A [4] [%]	$\langle E \rangle$ [6]	A_{fixed} [5]	
G_A:T_D	82.7	7.1	66.3	94.0	**0.066**	65.4	5.7	4.2	6.0	**0.23**	29.5	0.99
G_A:T_D-MutS	82.7	7.1	23.3	34.6	**0.066**	62.3	4.1	44	65.4	**0.28**	32.7	1.75
T_A:G_D	82.7	7.1	43.4	93.5	**0.066**	60.5	9.0	3	6.5	**0.32**	53.6	0.76
T_A:G_D-MutS	75	9.3	68.9	98.9	**0.11**	49.6	1.4	0.8	1.1	**0.60**	30.3	1.46
G_A:G_D	82.7	7.1	38.1	97.4	**0.066**	58.3	9.6	1	2.6	**0.37**	60.9	1.04
G_A:G_D-MutS	75	9.6	41.3	65.8	**0.11**	62.3	4.1	21.5	34.2	**0.28**	37.2	1.38
G_A:C_D	82.7	7.1	58.2	90.0	**0.066**	76.5	18.7	6.5	10.0	**0.10**	35.3	0.91
G_A:C_D-MutS	82.7	7.1	65.02	94.8	**0.066**	62.3	4.1	3.6	5.2	**0.28**	31.4	1.16

[1] $\langle R_{DA} \rangle_E$ corresponds to the FRET-averaged distance between the dyes, [2] **HW** to the half width of the distribution (see Supplementary Section 2.3.1).[3] **A** refers to the amplitude of a given population as given by the fit, [4] **rel. A** refers to the relative amplitude of the population in relation only to the FRET populations (D_{only} excluded). [5] A_{fixed} refers to the donor-only population, considered fixed at 110Å, [6] $\langle E \rangle$ corresponds to the FRET efficiency value for Förster radius of 53.2 Å and an interdye distance $\langle R_{DA} \rangle_E$.

Supplementary Table 1.8: **Nucleotide Effect**. Results of fits for which the FRET populations were fixed (Fitmodel 2) as described in the text (Supplementary section 2.3.1). LF: Blue background, MF: Orange background, HF: Magenta background, D_{only}: Light green background, Impurities: Dark brown background.

System	Model Function											χ_r^2
	State 1					State 2					D_{only}	
	$\langle R_{DA} \rangle_E$ [1] [Å]	HW[2] [Å]	A[3]	Rel. A[4] [%]	$\langle E \rangle$ [6]	$\langle R_{DA} \rangle_E$ [1] [Å]	HW[2] [Å]	A[3]	Rel. A[4] [%]	$\langle E \rangle$ [6]	A_{fixed} [5]	
G_A:T_D	82.7	7.1	71.3	98.2	**0.07**	58.1	5.6	1.3	1.8	**0.37**	27.4	1.38
G_A:T_D-MutS	82.7	7.1	16.6	24.7	**0.07**	62.3	4.1	51	75.3	**0.28**	32.7	1.51
G_A:T_D-MutS-AMP-PNP	82.7	7.1	70.9	97.3	**0.07**	58.5	3.2	2	2.7	**0.36**	27.1	1.56
G_A:T_D-MutS-ADP	75	9.6	18.2	24.4	**0.11**	63.2	3.5	56	75.6	**0.26**	25.5	0.92
G_A:T_D-MutS-ATP	82.7	7.1	18.4	25.0	**0.07**	64.2	4.5	55	75.0	**0.25**	26.4	0.91

[1] $\langle R_{DA} \rangle_E$ corresponds to the FRET-averaged distance between the dyes, [2] **HW** to the half width of the distribution (see Supplementary Section 2.3.1).[3] **A** refers to the amplitude of a given population as given by the fit, [4] **rel. A** refers to the relative amplitude of the population in relation only to the FRET populations (D_{only} excluded). [5] $\mathbf{A_{fixed}}$ refers to the donor-only population, considered fixed at 110Å, [6] $\langle E \rangle$ corresponds to the FRET efficiency value for Förster radius of 53.2 Å and an interdye distance $\langle R_{DA} \rangle_E$.

Supplementary Table 1.9: **Nucleotide effect.** The 95% confidence intervals of fits for which the FRET populations were fixed (Fitmodel 2) as described in the text (Supplementary Section 2.3.1). The parameters for which confidence intervals are not given were fixed during the fit. The χ_r^2-values corresponding to good fits are given for the case of the fits with Fitmodel 1 and 2 for direct comparison. The confidence intervals were calculated as described in Supplementary Section 2.3.2. Similar confidence intervals were obtained for the measurements not described in this table. LF: Blue background, MF: Orange background, HF: Magenta background, D_{only}: Light green background, Impurities: Dark brown background.

System	Model Function								χ_r^2	
	State 1				State 2					
	$\langle R_{DA}\rangle_E$ [1] [Å]	HW[2] [Å]	Rel. A[3] [%]	$\langle E\rangle$ [4]	$\langle R_{DA}\rangle_E$ [1] [Å]	HW[2] [Å]	Rel. A[3] [%]	$\langle E\rangle$ [4]	χ_r^2 (Fitmodel 2)	χ_r^2 (Fitmodel 1)
G_A:T_D	82.7	7.1	89.2-97.4	0.07	57.0-75.1	6.2-11.5	2.6-11.0	0.11-0.40	0.94-1.32	0.91-1.29
G_A:T_D-MutS	82.7	7.1	30.5-38.8	0.07	62.3	4.1	61.2-69.5	0.28	1.73-2.1	1.13-1.52
T_A:G_D-MutS	75	9.3	97.3-99.9	0.11	25.0-55.5	0.0-2.8	0.1-2.7	0.44-1.00	1.37-1.74	1.36-1.75
G_A:T_D-MutS-ADP	75	9.3	17.3-32.9	0.11	63.0-63.9	1.6-4.7	67.1-82.7	0.26-0.45	0.99-1.37	0.74-1.13
G_A:T_D-MutS-ATP	82.7	7.1	18.9-30.4	0.07	64.0-65.0	3.8-5.2	69.6-81.1	0.23-0.26	0.89-1.11	0.72-1.11

[1] $\langle R_{DA}\rangle_E$ corresponds to the FRET-averaged distance between the dyes, [2] **HW** to the half width of the distribution (see Supplementary Section 2.3.1).[3] **rel. A** refers to the relative amplitude of the population in relation only to the FRET populations (D_{only} excluded). [4] $\langle E\rangle$ corresponds to the FRET efficiency value for Förster radius of 53.2 Å and an interdye distance $\langle R_{DA}\rangle_E$.

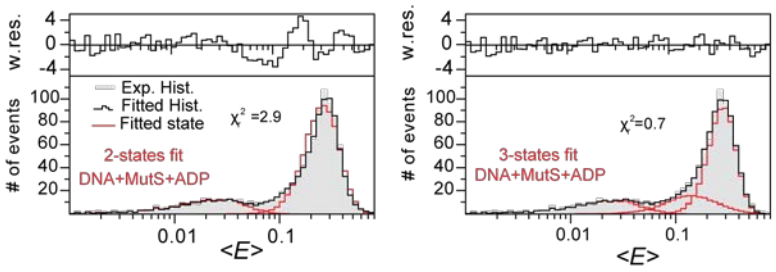

Supplementary Figure 1: 2-state fits vs. 3-state fits for the case of G_A:T_D-MutS-ADP. The F-test returns that the 3-state model is justified with 100% probability. For the rest of measurements the need for using a 3-state model instead of a 2-state model is even more pronounced.

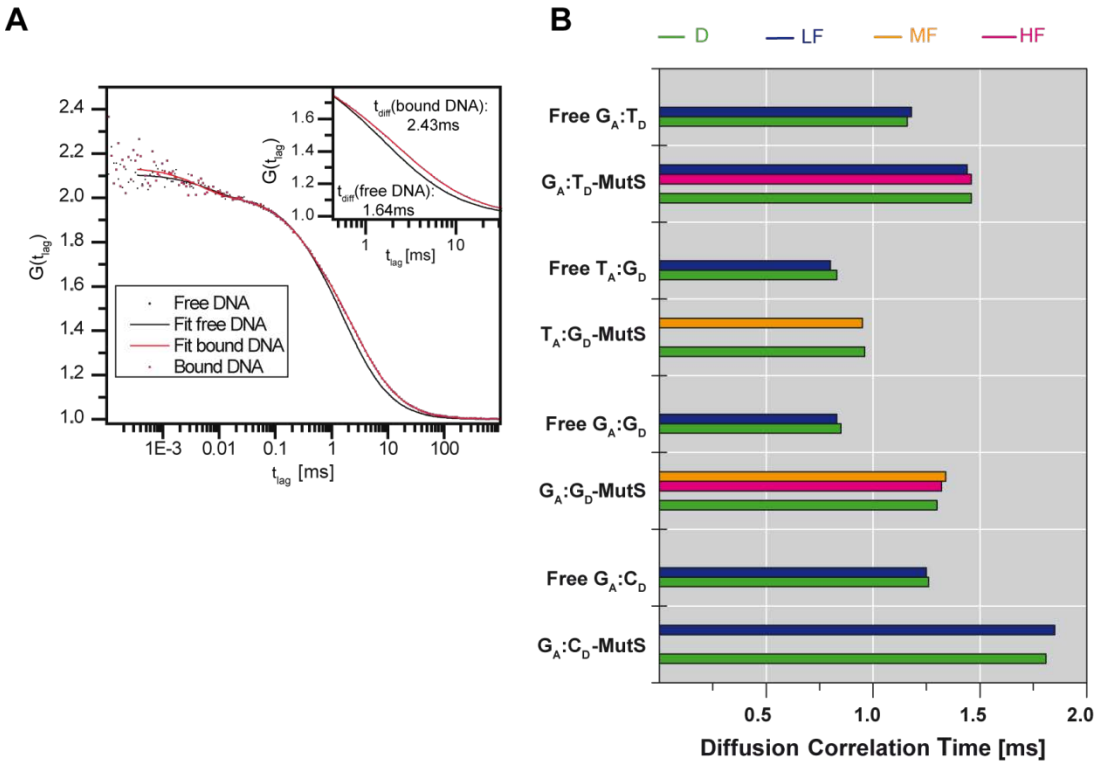

Supplementary Figure 2: Fluorescence correlation spectroscopy analysis of the smMFD data was used to determine and compare the diffusion times of the labeled DNA through the observation volume of each FRET species in the absence or presence of MutS. **A:** Typical correlation curves for the free and bound DNA oligonucleotides used in the single molecule measurements are shown in black and red correspondingly. **B:** Increased apparent diffusion correlation times in relation to the free DNA are indicative for the formation of a DNA-MutS complex. The color coding is the same as in the main text (Green: D-only, Blue: LF, Orange: MF, Magenta: HF).

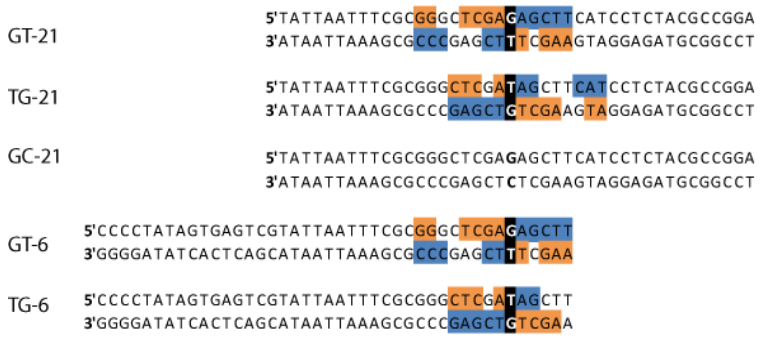

Supplementary Figure 3: Sequence of unlabeled duplex DNA used in the competition experiments shown in Fig. 6 in the main text. The mismatched bases are shown in white letters on black background. DNA-MutS contacts are indicated for the case that MutS stacks only to the mismatched T. Contacts made by subunit A of MutS are shown in blue, contacts of subunit B in orange. Note that in case of T:G-6-MutS interaction less contacts are made because the mismatch is too close to the DNA end.

References

58. Eggeling, C., Berger, S., Brand, L., Fries, J.R., Schaffer, J., Volkmer, A. and Seidel, C.A. (2001) Data registration and selective single-molecule analysis using multi-parameter fluorescence detection. *J Biotechnol*, 86, 163-180.

59. Eggeling, C., Widengren, J., Brand, L., Schaffer, J., Felekyan, S. and Seidel, C.A. (2006) Analysis of photobleaching in single-molecule multicolor excitation and Forster resonance energy transfer measurements. *J Phys Chem A*, 110, 2979-2995.

60. Clegg, R.M. (1992) Fluorescence resonance energy transfer and nucleic acids. *Methods in Enzymol*, 211, 353-388.

61. Eggeling, C., Schaffer, J., Seidel, C.A.M., Korte, J., Brehm, G., Schneider, S. and Schrof, W. (2001) Homogeneity, Transport, and Signal Properties of Single Ag Particles Studied by Single-Molecule Surface-Enhanced Resonance Raman Scattering. *J Phys Chem A*, 105, 3673-3679.

62. Lakowicz, J.R. (2006) *Principles of Fluorescence Spectroscopy*. Third ed. Springer, New York.

63. Koshioka, M., Sasaki, K. and Masuhara, H. (1995) Time-Dependent Fluorescence Depolarization Analysis in 3-Dimensional Microspectroscopy. *Applied Spectroscopy*, 49, 224-228.

64. Torella, J.P., Holden, S.J., Santoso, Y., Hohlbein, J. and Kapanidis, A.N. (2011) Identifying molecular dynamics in single-molecule FRET experiments with burst variance analysis. *Biophys J*, 100, 1568-1577.

65. Philip, B.R. and Robinson, D.K. (2002) *Data Reduction and Error Analysis for the Physical Sciences*. McGraw Hill.

66. Ehrenberg, M. and Rigler, R. (1974) Rotational brownian motion and fluorescence intensify fluctuations. *Chem Phys*, 4, 390-401.

67. Magde, D., Elson, E. and Webb, W.W. (1972) Thermodynamic Fluctuations in a Reacting System—Measurement by Fluorescence Correlation Spectroscopy. *Phys Rev Lett*, 29, 705.